REPORT DOCUMENTATION PAGE

Form Approved OMB NO. 0704-0188

1. REPORT DATE (DD-MM-YYYY)	2. REPORT TYPE	3. DATES COVERED (From - To)
	New Reprint	-

4. TITLE AND SUBTITLE
Quantitative image recovery from measured blind backscattered data using a globally convergent inverse method

5a. CONTRACT NUMBER
W911NF-11-1-0399

5b. GRANT NUMBER

5c. PROGRAM ELEMENT NUMBER
611102

5d. PROJECT NUMBER

5e. TASK NUMBER

5f. WORK UNIT NUMBER

6. AUTHORS
Andrey V. Kuzhuget, Larisa Beilina, Michael V. Klibanov, Anders Sullivan, Lam Nguyen, Michael A. Fiddy

7. PERFORMING ORGANIZATION NAMES AND ADDRESSES
University of North Carolina - Charlotte
Office of Sponsored Programs
9201 University City Blvd.
Charlotte, NC 28223 -0001

8. PERFORMING ORGANIZATION REPORT NUMBER

9. SPONSORING/MONITORING AGENCY NAME(S) AND ADDRESS(ES)
U.S. Army Research Office
P.O. Box 12211
Research Triangle Park, NC 27709-2211

10. SPONSOR/MONITOR'S ACRONYM(S)
ARO

11. SPONSOR/MONITOR'S REPORT NUMBER(S)
60035-MA.6

12. DISTRIBUTION AVAILABILITY STATEMENT
Approved for public release; distribution is unlimited.

13. SUPPLEMENTARY NOTES
The views, opinions and/or findings contained in this report are those of the author(s) and should not contrued as an official Department of the Army position, policy or decision, unless so designated by other documentation.

14. ABSTRACT
The goal of this paper is to introduce the application of a globally convergent inverse scattering algorithm to estimate dielectric constants of targets using time resolved backscattering data collected by a US Army Research Laboratory (ARL) forward looking radar. The processing of the data was conducted blind, i.e. without any prior knowledge of the targets. The problem is solved by formulating the scattering problem as a coefficient inverse problem for a hyperbolic partial differential equation. The main new feature of this algorithm is its rigorously

15. SUBJECT TERMS
joint paper with ARL engineers Anders Sullivan and Lam Nguyen, remote sensing, inverse scattering, quantitative imaging, experimental data

16. SECURITY CLASSIFICATION OF: a. REPORT	b. ABSTRACT	c. THIS PAGE	17. LIMITATION OF ABSTRACT	15. NUMBER OF PAGES	19a. NAME OF RESPONSIBLE PERSON
UU	UU	UU	UU		Michael Klibanov
					19b. TELEPHONE NUMBER 704-687-2645

Standard Form 298 (Rev 8/98)
Prescribed by ANSI Std. Z39.18

Report Title

Quantitative image recovery from measured blind backscattered data using a globally convergent inverse method

ABSTRACT

The goal of this paper is to introduce the application of a globally convergent inverse scattering algorithm to estimate dielectric constants of targets using time resolved backscattering data collected by a US Army Research Laboratory (ARL) forward looking radar. The processing of the data was conducted blind, i.e. without any prior knowledge of the targets. The problem is solved by formulating the scattering problem as a coefficient inverse problem for a hyperbolic partial differential equation. The main new feature of this algorithm is its rigorously established global convergence property. Calculated values of dielectric constants are in a good agreement with material properties, which were revealed a posteriori.

REPORT DOCUMENTATION PAGE (SF298)
(Continuation Sheet)

Continuation for Block 13

ARO Report Number 60035.6-MA
Quantitative image recovery from measured blin ...

Block 13: Supplementary Note

Quantitative Image Recovery From Measured Blind Backscattered Data Using a Globally Convergent Inverse Method

Andrey V. Kuzhuget, Larisa Beilina, Michael V. Klibanov, Anders Sullivan, Lam Nguyen, and Michael A. Fiddy

***Abstract*—The goal of this paper is to introduce the application of a globally convergent inverse scattering algorithm to estimate dielectric constants of targets using time-resolved backscattering data collected by a U.S. Army Research Laboratory forward-looking radar. The processing of the data was conducted blind, i.e., without any prior knowledge of the targets. The problem is solved by formulating the scattering problem as a coefficient inverse problem for a hyperbolic partial differential equation. The main new feature of this algorithm is its rigorously established global convergence property. Calculated values of dielectric constants are in a good agreement with material properties, which were revealed *a posteriori*.**

***Index Terms*—Experimental data, inverse scattering, quantitative imaging, remote sensing.**

I. Introduction

A FUNDAMENTAL problem in remote sensing is the processing of scattered field data from strongly scattering penetrable targets. Multiple scattering renders this problem extremely difficult to solve, it being ill conditioned with additional questions of uniqueness and, the most difficult, nonlinearity to contend with. In practice, limited noisy data typically require that some physical models be assumed, from which one hopes to extract meaningful and preferably quantitative information about the target in question. A number of recent publications by Beilina and Klibanov [3]–[8] and by Klibanov *et al.* [12], [14]–[16] have led to a new approach to address this important topic. This numerical method was originally developed for some multidimensional coefficient inverse problems (MCIPs) for a hyperbolic partial differential equation (PDE) using data from only a single location of either a point source or from a single direction of an incident plane wave. In particular, in [14], that method was extended from the 3-D case to the 1-D case. Thus, that 1-D version of [14] is used here to work with the experimental data. The illuminating field is pulsed in time, and the time history of the backscattering from the illuminated target volume constitutes the measured data that are processed by this algorithm. The authors are unaware of other groups working on MCIPs using data acquired from a single source location. However, the single measurement case is clearly the most practical one, particularly for military applications. Indeed, because of many dangers on the battlefield, the number of measurements should be minimized.

The algorithm in the aforementioned cited publications computes values for the spatial distribution of the dielectric constants of objects within the target volume. It is important to stress that this algorithm requires neither no prior knowledge of what might exist in the target volume nor a prior knowledge of a good first guess about the solution. There is a rigorous guarantee that this algorithm globally converges (see mathematical details in [7], [14], [16], and [17]). Because of the global convergence property, estimates of spatially distributed dielectric constants are reliable and systematically improve with more measured and less noisy data. The theory of the aforementioned cited publications rigorously guarantees that this numerical method delivers a good approximation to the exact solution of an MCIP without any *a priori* information about a small neighborhood of the exact solution as long as iterations start from the so-called “first tail function” $V_0(x)$, which can be easily computed using available boundary measurements (see (2.27)–(2.29) in Section II-C). In addition, it is in this sense that we use the term “global convergence" of the algorithm. The common perception of the term "global convergence" is that one can start from any point and still get the solution, but we stress that we actually start not from any point but rather from the function $V_0(x)$, which can be easily computed from the boundary data (see (2.27)–(2.29) in Section II-C).

It is well known that least squares functionals for MCIPs suffer from multiple local minima and ravines. Hence, local convergence of numerical methods to incorrect estimates will occur unless an initial guess that is close to the true solution is used. Such a guess is rarely available in most applications. In contrast, our algorithm does not use a least squares functional, and hence, it is free from the problem of local minima. Instead, this algorithm relies on the structure of the differential operator of the wave-like PDE.

Manuscript received March 24, 2012; revised July 22, 2012; accepted July 27, 2012. This work was supported in part by the U.S. Army Research Laboratory and the U.S. Army Research Office under Grant W911NF-11-1-0399; by the Swedish Research Council (VR); by the Swedish Foundation for Strategic Research (SSF) in Gothenburg Mathematical Modelling Centre; and by the Swedish Institute, Visby Program.

AQ1 A. V. Kuzhuget is with Morgan Stanley, New York, NY 10036 USA.

L. Beilina is with the Department of Mathematical Sciences, Chalmers University of Technology, 421 96 Gothenburg, Sweden, and also with Gothenburg University, 405 30 Gothenburg, Sweden (e-mail: larisa@chalmers.se).

M. V. Klibanov is with the Department of Mathematics and Statistics, University of North Carolina at Charlotte, Charlotte, NC 28223 USA (e-mail: mklibanv@uncc.edu).

A. Sullivan and L. Nguyen are with the U.S. Army Research Laboratory, Adelphi, MD 20783 USA (e-mail: anders.j.sullivan.civ@mail.mil; lam.h.nguyen2.civ@mail.mil).

M. A. Fiddy is with the Optoelectronics Center, University of North Carolina at Charlotte, Charlotte, NC 28223 USA (e-mail: mafiddy@uncc.edu).

Color versions of one or more of the figures in this paper are available online at http://ieeexplore.ieee.org.

Digital Object Identifier 10.1109/TGRS.2012.2211885

Prior to the work reported here, a major focus by the U.S. Army Research Laboratory (ARL) had been on the development of image processing techniques [19] that would improve radar images, which is through postprocessing techniques rather than through the application of inverse scattering methods. By incorporating more physics of the target-wave electromagnetic response into the data processing, one can greatly improve target detection and identification. Present data processing provides an electromagnetic field brightness or an intensity map of the target volume, which need not relate in a simple fashion to the scattering structures themselves. Our method estimates dielectric constants of targets, which obviously adds an important new dimension to the interpretation of data acquired by the radar system since this allows specific bounds on the dielectric properties of a feature in the target volume, which can help identify its likely material properties. Since no prior knowledge is required, the measured data were processed by Kuzhuget, Beilina, Klibanov, and Fiddy in the most challenging scenario, i.e., without any knowledge of the actual target structures and their dielectric properties. Once this had been done, Sullivan and Nguyen compared *a posteriori* the image estimates with the actually known material characteristics.

We draw attention to the fact that this algorithm has been used with forward-scattered data from experiments. These results were previously reported, which are also in a blind experiment (see [12, Tables 5 and 6] and [7, Tables 5.5 and 5.6]). In this case, the images in [12] were further improved and presented in a follow-up publication [6] using the adaptivity technique of [1], [2], [4], [5], and [7].

In Section II, we outline the basic steps in the underlying theory upon which the new algorithm is based. In Section III, we formulate the global convergence theorem. In Section IV, we outline results obtained using time-resolved backscatter electric field measurements collected in the field. Measurements were carried out by a forward-looking radar system built and operated by the ARL. The data were noisy and limited, and the target volumes included miscellaneous sources of clutter. The purpose of this particular radar system is to detect and possibly identify shallow explosive-like targets.

II. Theoretical Background

A. Integral Differential Equation

Since we were given only one time-resolved experimental curve per target, we had no choice but to use a 1-D mathematical model, although the reality is 3-D (see Section III for some details about the data collection). In addition, since only one component of the electric wave field was both transmitted and measured, we model the scattering process with one wave-like PDE rather than using complete Maxwell equations. We stress that the method is designed for use with 3-D problems, and one would normally collect data with co polarization and cross polarization in order to capture all of the pertinent information about the target. Here, we simply wish to show the steps employed by the method and demonstrate their quantitative reconstruction accuracy given noisy measured data.

We assume that the constitutive parameter of interest, i.e., mapping the target volume, is a relative permittivity $\varepsilon_r(x)$. In other words, we ignore magnetic effects in this paper. We also assume for convenience that $\varepsilon_r(x) = 1$ outside of the target volume, which is $x \in (0, 1)$ in our case. We assume that the source $x_0 < 0$ lies outside of the target volume. We can write the forward scattering problem as

$$\varepsilon_r(x)u_{tt} = u_{xx}, \qquad x \in \mathbb{R} \tag{2.1}$$
$$u(x,0) = 0, \quad u_t(x,0) = \delta(x - x_0). \tag{2.2}$$

The subscripts in (2.1) indicate the number of partial derivatives with respect to the variable indicated. The coefficient inverse problem (CIP) is to recover $\varepsilon_r(x)$, assuming that the initial illuminating pulse is known and that we measure the function $g(t)$, i.e.,

$$u(0,t) = g(t) \tag{2.3}$$

for sufficiently large times t that all multiple scattering events within the target volume, which can produce a measurable signal at the detector, do so. Practically, we gate the radiation source in time; and since the Laplace transform (LT), i.e., $w(x,s)$, is used to solve this CIP, the decay $e^{-st}, s > 0$ of the LT kernel further limits the duration of the measured time history. It is worth pointing out that, more typically, scattering data would be measured at different scattering angles for fixed frequency illumination at various incident angles. One can easily appreciate that this leads to the acquisition of Fourier information about the target or the secondary source function, depending upon the extent of the multiple scattering; and once one has sufficient data, a reasonable estimate of the target properties becomes possible. By taking measurements in the time domain, one can see that this is essentially simultaneously gathering information in a transform space from many illumination frequencies. The Laplace and Fourier transforms provide complimentary representations of the target in terms of moments or modes, respectively.

The LT is

$$w(x,s) = \int_0^\infty u(x,t)e^{-st}dt := \mathcal{L}u, \qquad s \geq \underline{s} = \text{const.} > 0 \tag{2.4}$$

and we assume that the so-called pseudofrequency $s \geq s(\varepsilon_r(x)) := \underline{s}$ is sufficiently large. This gives [7]

$$w_{xx} - s^2\varepsilon_r(x)w = -\delta(x - x_0), \qquad x \in \mathbb{R} \tag{2.5}$$
$$\lim_{|x|\to\infty} w(x,s) = 0. \tag{2.6}$$

Let

$$w(0,s) = \varphi(s) = \mathcal{L}g \tag{2.7}$$

be the LT of the measured function $g(t)$ in (2.3). Since $\varepsilon_r(x) = 1$ for $x < 0$, then, using (2.5) and (2.6), one can prove that, in addition to the function $w(0,s)$ in (2.7), the function $w_x(0,s)$ is also known as (see [17])

$$w_x(0,s) = s\varphi(s) - \exp(sx_0). \tag{2.8}$$

Let $w_0(x,s)$ be the solution of the problem in (2.5) and (2.6) for the case of the uniform background $\varepsilon_r(x) \equiv 1$. Then

$$w_0(x,s) = \frac{\exp\left(-s|x-x_0|\right)}{2s}. \tag{2.9}$$

When implementing the algorithm, given the assumption of a uniform normalized $\varepsilon_r(x) = 1$ outside of the target volume, we consider the function

$$r(x,s) = \frac{1}{s^2}\ln\left(\frac{w}{w_0}(x,s)\right). \tag{2.10}$$

Since the source $x_0 < 0$, then the function $r(x,s)$ is the solution of the following equation in the interval (0, 1):

$$r_{xx} + s^2 r_x^2 - 2sr_x = \varepsilon_r(x) - 1, \qquad x \in (0,1). \tag{2.11}$$

In addition, by (2.7) and (2.8)

$$r(0,s) = \varphi_0(s), \quad r_x(0,s) = \varphi_1(s) \tag{2.12}$$

$$\varphi_0(s) = \frac{\ln\varphi(s) - \ln(2s)}{s^2} + \frac{x_0}{s}$$

$$\varphi_1(s) = \frac{2}{s} - \frac{e^{sx_0}}{s^2\varphi(s)}. \tag{2.13}$$

The idea now is to eliminate the unknown coefficient $\varepsilon_r(x)$ from (2.11) via differentiation with respect to pseudofrequency s. Differentiating (2.11) with respect to s and denoting $q(x,s) = \partial_s r(x,s)$, we obtain

$$q_{xx} + 2s^2 q_x r_x + 2sr_x^2 - 2sq_x - 2r_x = 0, \qquad x \in (0,1). \tag{2.14}$$

We now need to express in (2.14) the function r via the function q. We have

$$r(x,s) = -\int_s^{\overline{s}} q(x,\tau)d\tau + V(x,\overline{s}) \tag{2.15}$$

where $V(x) := V(x,\overline{s})$ is referred to as the *tail function*, which is small in practice for large positive $\overline{s}$. Here, the truncation pseudofrequency $\overline{s}$ serves as a regularization parameter. The exact formula for $V(x)$ is

$$V(x,\overline{s}) := V(x) = r(x,\overline{s}) = \frac{1}{\overline{s}^2}\ln\left(\frac{w(x,\overline{s})}{w_0(x,\overline{s})}\right). \tag{2.16}$$

Substituting (2.15) in (2.14), we obtain the following nonlinear integral differential equation:

$$\begin{aligned} q_{xx} &- 2s^2 q_x \int_s^{\overline{s}} q_x(x,\tau)d\tau + 2s\left[\int_s^{\overline{s}} q_x(x,\tau)d\tau\right]^2 \\ &- 2sq_x + 2\int_s^{\overline{s}} q_x(x,\tau)d\tau \\ &+ 2s^2 q_x V_x - 4sV_x \int_s^{\overline{s}} q_x(x,\tau)d\tau \\ &+ 2s(V_x)^2 - 2V_x = 0, \end{aligned} \tag{2.17}$$

$$\begin{aligned} &x \in (0,1); \quad s \in [\underline{s}, \overline{s}] \\ &q(0,s) = \psi_0(s), \quad q_x(0,s) = \psi_1(s) \\ &q_x(1,s) = 0, \qquad s \in [\underline{s}, \overline{s}] \end{aligned} \tag{2.18}$$

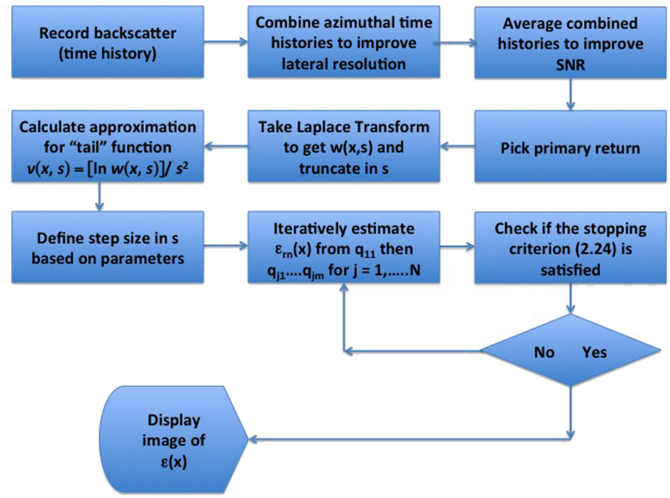

Fig. 1. Flowchart of the algorithm.

where functions $\psi_0(s) = \varphi_0'(s)$ and $\psi_1(s) = \varphi_1'(s)$ are derived from (2.13). The condition $q_x(1,s) = 0$ can be easily derived from (2.6) since $\varepsilon_r(x) = 1$ outside of the interval (0, 1).

In (2.17) and (2.18), both functions $q(x,s)$ and $V(x)$ are unknown. The reason why we can approximate both of them is that we find updates for $q(x,s)$ via inner iterations exploring (2.17) and (2.18) inside of the interval (0, 1). At the same time, we update the tail function $V(x)$ via outer iterations exploring the entire real line $\mathbb{R}$. In short, given an approximation for $V(x)$, the algorithm updates q and then updated for $\varepsilon_r(x)$. Next, the forward problem in (2.5) and (2.6) is solved for the function $w(x,s)$ for $s = \overline{s}$. Next, the tail function $V(x)$ is updated using (2.16). This might seem reminiscent of the steps in algorithms such as the modified gradient inverse scattering technique [20]; but we emphasize that, unlike our case, such methods have no global convergence properties.

B. Iterative Process

We now outline the formulation of our algorithm and the iterative process (see details in [7], [14], [16], and [17]; see Fig. 1). Unlike computationally simulated data in [14], we do not use prior knowledge of the function $q(1,s)$ on the transmitted edge since this function is unknown to us. We have observed in our computational experiments that the knowledge of $q(1,s)$ only affects the accuracy of the calculation of the location of the target, but it does not affect the accuracy of the computed target/background contrast. Here, we are interested only in that contrast (see Section III). Since $\varepsilon_r(x) = 1$ for $x \geq 1$ and $x_0 < 0$, then one can easily derive from equations (2.5), (2.9), and (2.10) that $\partial_x q(1,s) = 0$.

Consider a partition of the interval $[\underline{s}, \overline{s}]$ into N small subintervals with the small grid step size $h > 0$ and assume that the function $q(x,s)$ is piecewise constant with respect to s. Thus

$$\begin{aligned} &\underline{s} = s_N < s_{N-1} < \cdots < s_0 = \overline{s}, \qquad s_{i-1} - s_i = h \\ &q(x,s) = q_n(x), \qquad \text{for } s \in (s_n, s_{n-1}]. \end{aligned} \tag{2.19}$$

For each subinterval $(s_n, s_{n-1}]$ we obtain a differential equation for the function $q_n(x)$. We assign, for convenience of notations, $q_0 :\equiv 0$. Following the aforementioned idea of a combination of inner and outer iterations, we perform for each n inner iterations

with respect to the tail function. This way, we obtain functions $q_{n,k}$ and $V_{n,k}$. The equation for the pair $(q_{n,k}, V_{n,k})$ is

$$
\begin{aligned}
&q''_{n,k} - \left(A_{1,n} h \sum_{j=0}^{n-1} q'_j - A_{1,n} V'_{n,k} - 2A_{2,n} \right) q'_{n,k} \\
&\quad = -A_{2,n} h^2 \left(\sum_{j=0}^{n-1} q'_j \right)^2 + 2h \sum_{j=0}^{n-1} q'_j + 2A_{2,n} V'_{n,k} \left(h \sum_{j=0}^{n-1} q'_j \right) \\
&\qquad - A_{2,n} \left(V'_{n,k} \right)^2 + 2A_{2,n} V'_{n,k}, \qquad x \in (0,1) \qquad (2.20)\\
&q_{n,k}(0) = \psi_{0,n}, \quad q'_{n,k}(0) = \psi_{1,n}, \quad q'_{n,k}(1) = 0 \qquad (2.21)\\
&\psi_{0,n} = \frac{1}{h} \int_{s_n}^{s_{n-1}} \psi_0(s) ds, \quad \psi_{1,n} = \frac{1}{h} \int_{s_n}^{s_{n-1}} \psi_1(s) ds.
\end{aligned}
$$

Here, $A_{1,n}$ and $A_{2,n}$ are certain numbers, whose exact expressions are given in [3] and [7].

The choice of the first tail function $V_0(x)$ is described in Section II-C. Let $n \geq 1$. Suppose that, for $j = 0, \ldots n-1$, functions $q_j(x)$ and $V_j(x)$ are already constructed. We now need to construct functions $q_{n,k}$ and $V_{n,k}$ for $k = 1, \ldots, m$. We set $V_{n,1}(x) := V_{n-1}(x)$. Next, using the quasi-reversibility method (QRM) (see Section II-C), we approximately solve (2.20) for $k = 1$ with overdetermined boundary conditions in (2.21) and find the function $q_{n,1}$. Next, we find the approximation $\varepsilon_r^{(n,1)}$ for the unknown coefficient $\varepsilon_r(x)$ via the following two formulas:

$$
\begin{aligned}
r_{n,1}(x) &= -hq_{n,1} - h \sum_{j=0}^{n-1} q_j + V_{n,1}, \qquad x \in [0,1] \qquad (2.22)\\
\varepsilon_r^{(n,1)}(x) &= 1 + r''_{n,1}(x) + s_n^2 \left[r'_{n,1}(x) \right]^2 \\
&\quad - 2s_n r'_{n,1}(x), \qquad x \in [0,1]. \qquad (2.23)
\end{aligned}
$$

Next, we solve the forward problem in (2.5) and (2.6) with $\varepsilon_r(x) := \varepsilon_r^{(n,1)}(x), \quad s := \overline{s}$ and find the function $w_{n,1}(x, \overline{s})$ this way. After this, we update the tail via the formula in (2.16), in which $w(x, \overline{s}) := w_{n,1}(x, \overline{s})$. This way, we obtain a new tail $V_{n,2}(x)$. Similarly, we continue iterating with respect to tails m times. Next, we set

$$
q_n(x) := q_{n,m}(x), \; V_n(x) := V_{n,m}(x), \; \varepsilon_r^{(n)}(x) := \varepsilon_r^{(n,m)}(x)
$$

replace n with $n+1$ and repeat this process. We continue this process until [15]

$$
\text{either } \left\| \varepsilon_r^{(n)} - \varepsilon_r^{(n-1)} \right\|_{L_2(0,1)} \leq 10^{-5} \quad \text{or } \left\| \nabla J_\alpha(q_{n,k}) \right\|_{L_2(0,1)} \geq 10^5 \qquad (2.24)
$$

where the functional $J_\alpha(q_{n,k})$ is defined in Section II-C. Here, the norm in the space $L_2(0,1)$ is understood in the discrete sense. In the case when the second inequality in (2.24) is satisfied, we stop at the previous iteration, taking $\varepsilon_r^{(n,k-1)}(x)$ as our solution. If neither of two conditions in (2.24) is not reached at $n := N$, then we repeat the aforementioned sweep over the interval $[\underline{s}, \overline{s}]$, taking the pair $(q_N(x), V_N(x))$ as the new pair $(q_0(x), V_0(x))$. Usually, at least one of the conditions in (2.24) is reached either on the third or on the fourth sweep, and the process stops then.

C. Computing Functions $q_{n,k}(x)$ and $V_0(x)$

At first glance, it seems that, for a given tail function $V_{n,k}(x)$, the function $q_{n,k}(x)$ can be computed as the solution of a conventional boundary value problem for the ordinary differential equation in (2.20) with any two out of three boundary conditions in (2.21). However, attempts to do so led to poor quality images (see [14, Remark 3.1]). At the same time, the QRM has resulted in accurate solutions both in [14] and in Test 1 for synthetic data (see succeeding discussion). The QRM is well designed to compute least squares solutions of PDEs with overdetermined boundary conditions, such as, e.g., the problem in (2.20) and (2.21). We refer to [18] for the originating work about the QRM and to [7], [9], [13], [15], and [16] for some follow-up publications.

Let $L(q_{n,k})(x)$ and $P_{n,k}(x)$ be left- and right-hand sides of (2.20), respectively. In our numerical studies, $L(q_{n,k})(x)$ and $P_{n,k}(x)$ are written in the form of finite differences. Let $\alpha \in (0,1)$ be the regularization parameter. The QRM minimizes the following Tikhonov regularization functional:

$$
J_\alpha(q_{n,k}) = \| L_{n,k}(q_{n,k}) - P_{n,k} \|^2_{L_2(0,1)} + \alpha \| q_{n,k} \|^2_{H^2(0,1)} \qquad (2.25)
$$

subject to boundary conditions in (2.21). Here, again norms in $L_2(0,1)$ and in the Sobolev space $H^2(0,1)$ are understood in the discrete sense. The functional $J_\alpha(q_{n,k})$ in (2.25) is quadratic. Using this fact and the tool of Carleman estimates, it can be shown that $J_\alpha(q_{n,k})$ has a unique global minimum and no local minima [14], [15], [17]. We find that global minimum via the conjugate gradient method, minimizing with respect to the values of the function $q_{n,k}$ at grid points. We have used 100 grid points in the interval (0, 1). The step size in the s-direction was $h = 0.5$. The s-interval was $[\underline{s}, \overline{s}] = [3, 12]$. For each $n = 1, \ldots, N$, we take functions $q_{n,k}$ for $k = 1, \ldots m$, and we typically choose $m = 10$. The reason for the choice of $m = 10$ is that numerical experience has shown that, for each of the n, tails stabilize at $k \approx 10$. As to the regularization parameter α, we have found, when testing synthetic data, that $\alpha = 0.04$ is the optimal one, and we take it in our computations.

We note that we determined the regularization parameter when testing simulated data. These data were for the target depicted in Fig. 7(a), for which we varied the regularization parameter between 0.03 and 0.05. The resulting images for these data showed only an insignificant change. We also varied the regularization parameter between 0.03 and 0.05 for the experimental data. Again, we only observed insignificant changes, which lead us to select the average value of 0.04. Although the regularization theory states that the regularization parameter should depend on the noise level in the data [23], we do not actually know the noise level for our data. Further, for nonlinear problems (as we have), this dependence is claimed by regularization theory only for the limiting case of a relatively small level of noise, which is not our case. In our computations using measured data, one works with some level of noise, which is not likely to be small and is unknown. Therefore, in practice, when applying this algorithm to experimental data, we were guided by results from simulations to choose a value for the regularization parameter. If we had prior knowledge about some objects in the target volume, then we would choose the optimal

regularization parameter for that object. Because we processed the data without any prior knowledge whatsoever about the objects, we chose the regularization parameter based on the simulated data processing, and fortunately, our answers for five out of five targets were well within tabulated limits.

We now describe an important step in choosing the first tail function $V_0(x)$. To choose it, we consider the asymptotic behavior of the function $V(x,\overline{s})$ in (2.16) with respect to the truncation pseudofrequency $\overline{s} \to \infty$. This behavior is [14], [17]

$$V(x,\overline{s}) = \frac{p_0(x)}{\overline{s}} + O\left(\frac{1}{\overline{s}^2}\right), \qquad \overline{s} \to \infty.$$

We truncate the term $O(1/\overline{s}^2)$, which is somewhat similar with the defining of geometrical optics as a high-frequency approximation of the solution of the Helmholtz equation. Hence, we take

$$V(x,\overline{s}) \approx \frac{p_0(x)}{\overline{s}}.$$

Since $q = \partial_s r$ and $V(x,\overline{s}) = r(x,\overline{s})$, then

$$q(x,\overline{s}) = -\frac{p_0(x)}{\overline{s}^2}. \tag{2.26}$$

Hence, setting in (2.17) $s := \overline{s}$ and using (2.26), we obtain the following *approximate* equation for the function $p_0(x)$:

$$\frac{d^2}{dx^2}p_0(x) = 0, \qquad x \in (0,1). \tag{2.27}$$

Boundary conditions for $p_0(x)$ can be easily derived from (2.18) and (2.26) as

$$p_0(0) = -\overline{s}^2\psi_0(\overline{s}),\ p_0'(0) = -\overline{s}^2\psi_1(\overline{s}),\ p_0'(1) = 0. \tag{2.28}$$

We find an approximate solution $p_{0,appr}(x)$ of the problem in (2.27) and (2.28) via the QRM, similarly with the aforementioned equation. Next, we set for the first tail function, i.e., AQ4

$$V_0(x) := \frac{p_{0,appr}(x)}{\overline{s}}. \tag{2.29}$$

A simplified formal statement of the global convergence theorem is as follows (see [7, Th. 6.1] for more details and [7, Th. 6.7] for the 3-D case).

Theorem 1: Let the function $\varepsilon_r^*(x)$ be the exact solution of our CIP for the noiseless data $g^*(t)$ in (2.3). Fix the truncation pseudofrequency $\overline{s} > 1$. Let the first tail function $V_0(x)$ be defined via (2.27)–(2.29). Let $\sigma \in (0,1)$ be the level of the error in the boundary data, i.e.,

$$|\psi_0(s) - \psi_0^*(s)| \le \sigma,\ |\psi_1(s) - \psi_1^*(s)| \le \sigma, \qquad \text{for } s \in [\underline{s}, \overline{s}]$$

where functions $\psi_0(s)$ and $\psi_1(s)$ depend on the function $g(t)$ in (2.3) via (2.7), (2.13) and (2.18); and functions $\psi_0^*(s)$ and $\psi_1^*(s)$ depend on the noiseless data $g^*(t)$ in the same way. Let $h \in (0,1)$ be the grid step size in the s-direction in (2.19); let $\sqrt{\alpha} = \sigma$ and $\widetilde{h} = \max(\sigma, h)$. Let Q be the total number of functions $\varepsilon_r^{(n,k)}$ computed in the aforementioned algorithm. Then, there exists a constant $D = D(x_0, d, \overline{s}) > 1$ such that, if the numbers σ and h are so small, that

$$\widetilde{h} < \frac{1}{D^{2Q+2}} \tag{2.30}$$

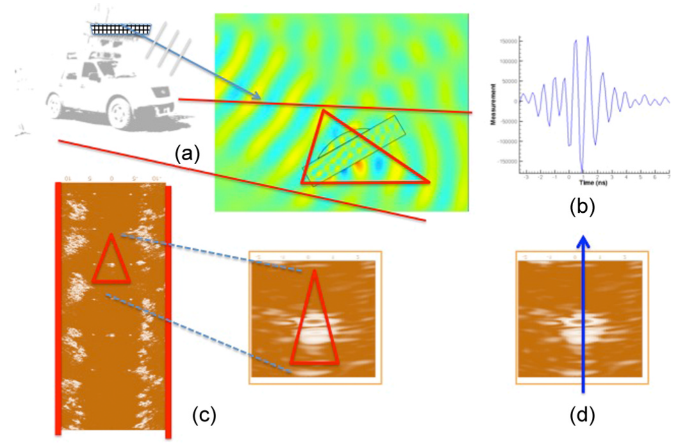

Fig. 2. (a) Schematic diagram of the forward-looking radar system illuminating a dielectric target. (b) Typical measured time history of the backscatter field. (c) Composite of unprocessed returns highlighting the dielectric target (indicated by the red triangle). (d) Downrange cut of the permittivity profile, which the new algorithm will generate.

then the following estimate is valid:

$$\left\|\varepsilon_r^{(n,k)} - \varepsilon_r^*\right\|_{L_2(0,1)} \le \widetilde{h}^{\omega} \tag{2.31}$$

where the number $\omega \in (0,1)$ is independent of n, k, $\widetilde{h}$, $\varepsilon_r^{(n,k)}$, and ε_r^*.

Therefore, Theorem 1 guarantees that, if the total number Q of computed functions $\varepsilon_r^{(n,k)}$ is fixed and error parameters σ, h are sufficiently small, then obtained iterative solutions $\varepsilon_r^{(n,k)}(x)$ are sufficiently close to the exact solution $\varepsilon_{r,}^*$; and this closeness is defined by the error parameters. Therefore, the total number of iterations Q can be considered as the regularization parameter of our process, which is the additional regularization parameter to the number $\overline{s}$. The combination of inequalities in (2.30) and (2.31) has a direct analog in the inequality in [11, Lemma 6.2, p. 156] for classical Landweber iterations, which are defined for a substantially different ill-posed problem. As to the total number of iterations Q being a regularization parameter here, there is no surprise in this. Indeed, it is stated on [11, p. 157] that the number of iterations can serve as a regularization parameter for an ill-posed problem.

III. Imaging Results

The schematic of the data collection by the forward-looking radar is shown in Fig. 2(a). Time-resolved electromagnetic pulses are emitted by two sources installed on the radar. Only one component of the electric field is both transmitted and measured in the backscatter direction. The data are collected by sixteen detectors with the step size in time of 0.133 ns. Data from shallow targets placed both below and above the ground were provided. The only piece of information provided by the ARL team (Sullivan and Nguyen) to Kuzhuget, Beilina, Klibanov, and Fiddy was whether the target was located above the ground or was buried. The depth of the upper surface of a buried target was a few centimeters. GPS was used to provide the distance between the radar and a point on the ground, which is located above that target to within a few centimeters error.

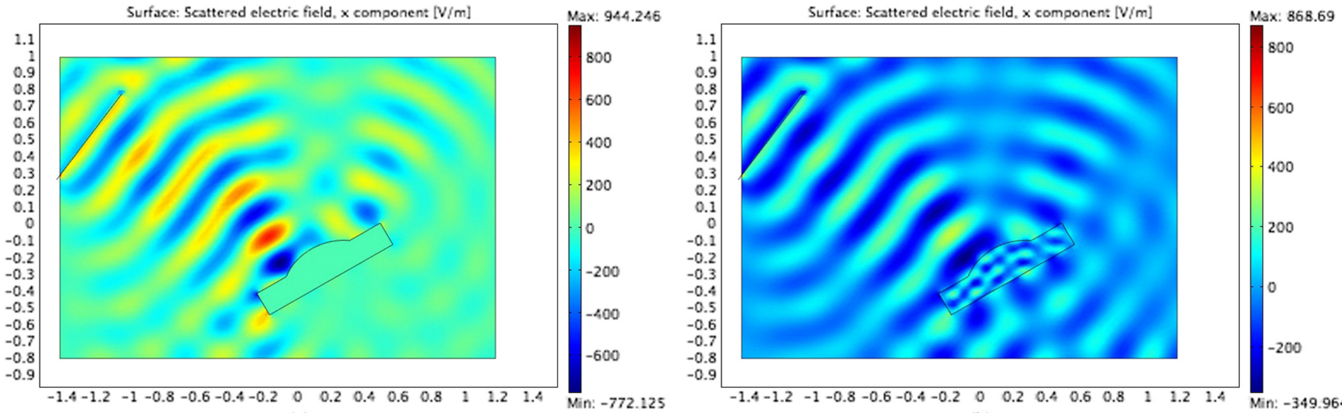

(a) (b)

Fig. 3. (a) Scattered field from a metallic target. (b) Scattered field from a high-permittivity target with the same shape ($\varepsilon_r(\text{target}) = 10$). Note the similarity between the backscatter electric fields in cases (a) and (b).

The time-resolved voltages induced by the backreflected signals were integrated over the radar to target distances ranging from 8 to 20 m, and they were also averaged with respect to both source positions and with respect to the output of the 16 detectors. Since we can assume here that the radar/target distance was known, then it was also approximately known which part of the measured time-resolved signal would correspond to scattering events from that target (see Fig. 2). Despite the presence of clutter, a single time-dependent curve is extracted from the measured return time histories, as illustrated in Fig. 2(b). This is the form of the data that have been processed in each of the five measured data sets generated by the ARL. A typical plot of returns without applying the inverse algorithm is shown in Fig. 2(c), where the triangle denotes a possible target of interest among the clutter from the backscatter generated from the volume of the region illuminated by the radar in Fig. 2(a). We process a set of averaged time histories like those shown in Fig. 2(b) to create a down-range cut of the permittivity profile, as indicated in Fig. 2(d).

Our objective was to calculate ratios

$$R = \frac{\varepsilon_r(\text{target})}{\varepsilon_r(\text{background})} \tag{3.1}$$

of dielectric constants. If the $\varepsilon_r(\text{background})$ is known, then it is trivial to deduce $\varepsilon_r(\text{target})$. Clearly, for a target located above the ground, $\varepsilon_r(\text{background}) = 1$. In general, we would expect the target volume to contain many inhomogeneities with spatially varying $\varepsilon_r(x)$. A weighted average of dielectric constants of these constituent materials will be found over the volume spatial resolution cell that corresponds to the particular data acquisition configuration. In the examples presented here, we show results obtained from just one time-history curve for each target, corresponding to one polarization component of the incident electromagnetic field and backscatter data measured and averaged over all 16 receiver locations. Clearly, this severely limits the transverse resolution but improves the signal-to-noise ratio for 1-D imaging in the propagation direction. The model is further simplified by using the 1-D CIP employing only one hyperbolic PDE. Consequently, the interpretation of the backscattering radiation will assign a high-permittivity value to metal structures. A comparison between Fig. 3(a) and (b) illustrates this. We use the upper bound $\varepsilon_r(\text{target}) = 30$ for the metallic targets because our calculations show that LT in (2.7), from the response function $g(t)$, almost coincides for $\varepsilon_r(\text{target}) \geq 30$.

In both cases of a metal structure and a high-permittivity structure, one can expect enhanced backscatter if the incident pulse includes frequencies that correspond to a normal mode of the target. Hence, we assign

$$10 \leq \varepsilon_r(\text{metallic target}) \leq 30. \tag{3.2}$$

We call (3.2) the appearing dielectric constant of metallic targets. In other words, we consider in (3.2) that regions appearing to have a high dielectric constant could also be metallic targets.

To appreciate the kind of backscatter data and image recovery expected from a simple dielectric block, a 1-D example illustrated in Fig. 3 was investigated. Computations in this example were performed using the software package WavES [24]. The permittivity profile, i.e., $\varepsilon_r(\text{target}) = 4$, is shown in Fig. 4(a); and the computed function $u(0,t) = g(t)$ for $0 < t < 3$ is shown in Fig. 4(b) [see (2.3) for $g(t)$]. We assume temporal units here for which at $t = 3$, a distance of $x = 3$ units is traversed; the source is at $x_0 = -1$, and the block's front face is at $x = 0.2$. Since the block is 0.2 units wide, $g(t)$ represents the backscatter return from the front and back face of the block. The reason why, in Fig. 4(b), $g(t) = 0$ for $t < 1$ and $g(t) = 1/2$ for $1 \leq t \leq 1.4$ is that the solution of the problem in (2.1) and (2.2) for $\varepsilon_r(x) \equiv 1$ is $u_0(x,t) = H(t - |x - x_0|)/2$, where $H(z)$ is the Heaviside function, i.e.,

$$H(z) = \begin{cases} 0, z < 0 \\ 1, z \geq 0. \end{cases}$$

Hence, $u(0,t) = g(t) = H(t-1)/2$ for $1 \leq t \leq 1.4$; and at $t = 1.4$, the return wave from the block hits the observation point $\{x = 0\}$ for the first time.

The measured data are also challenging to process since they arise from oblique illumination, and the exact location and the amplitudes of the incident pulses were not known. In addition, a comparison of Fig. 4(b) with Fig. 5(b), (d), and (f) shows that the measured data are highly oscillatory, which are unlike their simulated counterparts. Consequently, we applied

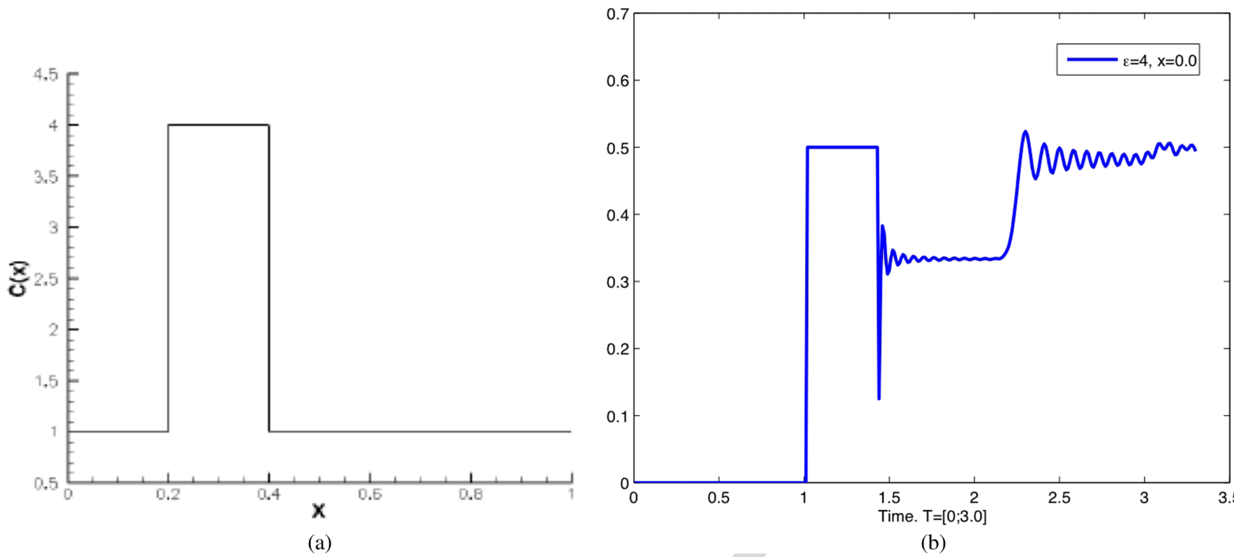

Fig. 4. (a) Function $\varepsilon_r(\text{target}) = 4$; note that $\varepsilon_r(\text{background}) = 1$. (b) $u(0,t) = g(t)$ for $0 < t < 3.0$. The source is located at $x_0 = -1$, and the first backscatter return is therefore shown at approximately $t = 2.4$ with "ringing" determined by interference of multiply scattered waves between the two boundaries of the block. Computations were performed using the software package WavES [24].

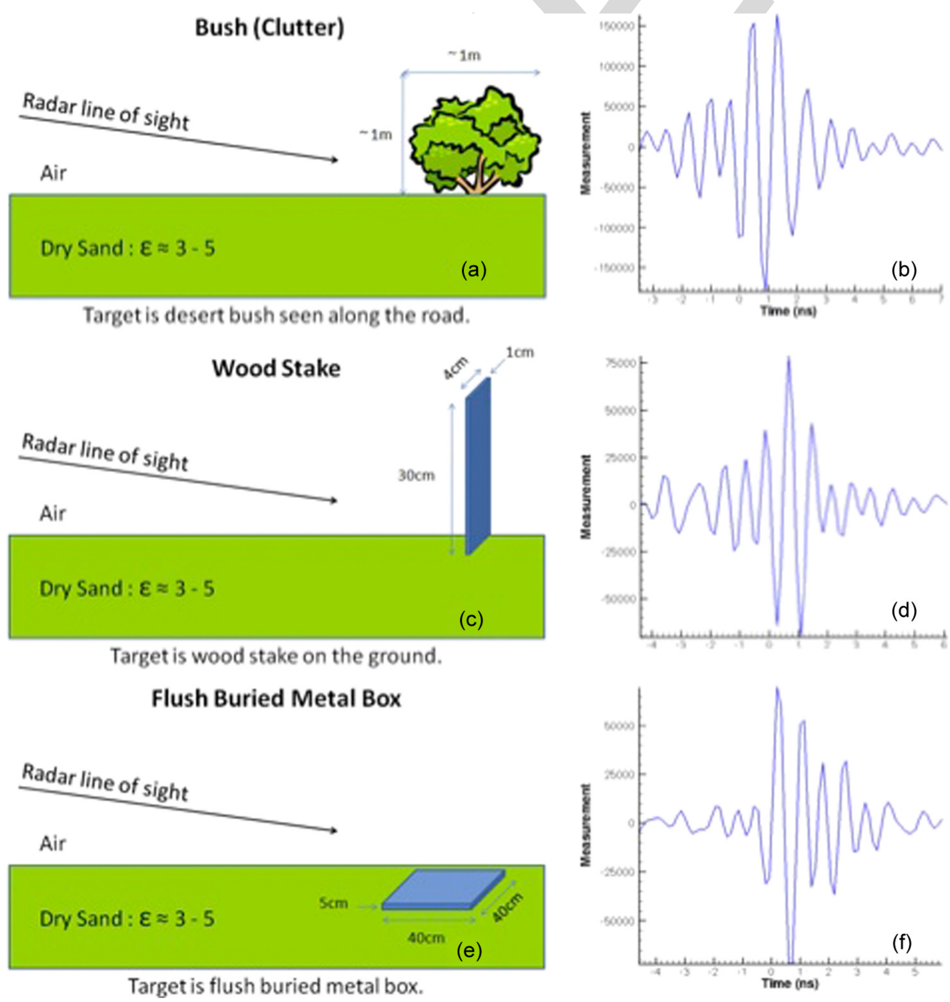

Fig. 5. Three targets and their associated measured data. The ground is dry sand with $3 \leq \varepsilon_r \leq 5$ [21], [22]. The information shown in (a), (c), and (e) were only provided after computations were made. (a) Depicts a bush that was located on a road, which generated background clutter. (b) Scaled experimental data for (a), where the horizontal axis represents time in nanoseconds having a time step of 0.133 ns; and the vertical axis is the amplitude of the measured voltage at the detector. (c) Wooden stake. (d) Scaled experimental data for (c). (e) Metal box buried in dry sand. (f) Scaled experimental data for (e). The mismatch between experimental and simulated data [see Fig. 4(b)] is evident.

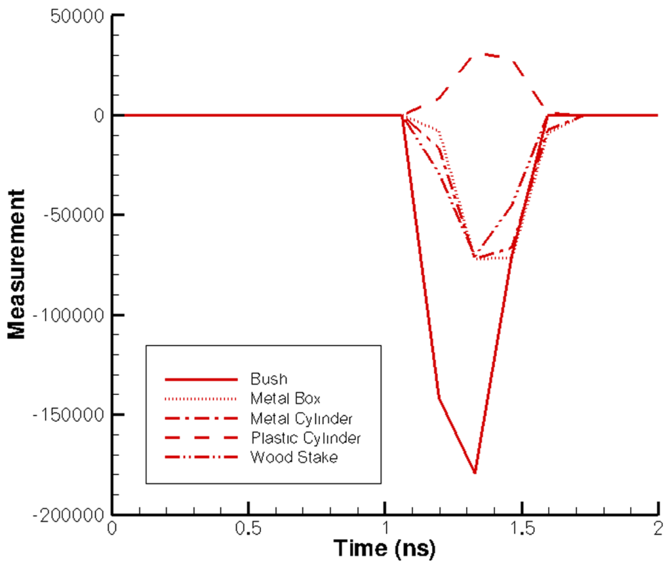

Fig. 6. Superimposed preprocessed data for all five cases under consideration. The upward-looking peak corresponds to the plastic cylinder (see Table I).

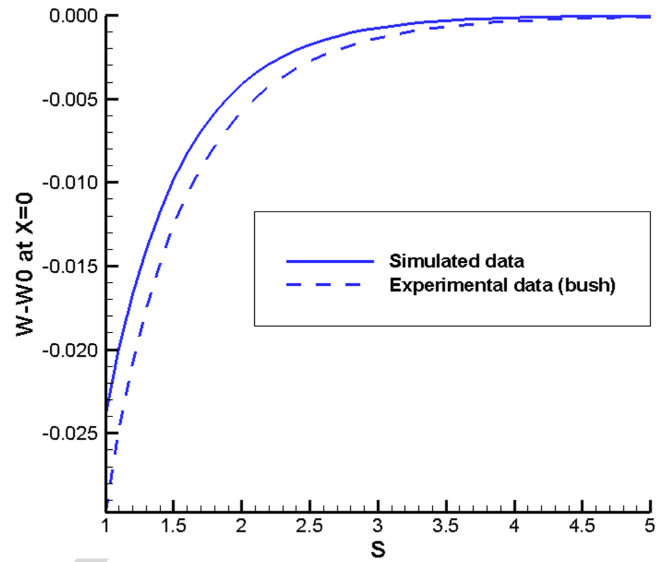

Fig. 7. Graphs of the function $\widehat{w}(0,s) = w(0,s) - w_0(0,s)$ for $s \in [1,5]$ for the LT of the computationally simulated data in Fig. 4(b) and of the preprocessed signal for the bush (see Fig. 6). The signal in Fig. 6 for the bush was multiplied by 10^{-7}. Minimal and maximal values of the function $\widehat{w}(0,s)$ are similar for both curves. A similar observation was made for four other targets we have worked with.

an intuitively reasonable data preprocessing procedure, which remained totally unbiased since it was applied to blind data sets. The idea of this procedure is to make the data more similar to that shown in Fig. 4(b). Previously, a similar procedure was reported for transmitted data in [6], [7], and [12]. We have considered two cases.

Case 1. Suppose that the target is located above the ground. In this case

$$\varepsilon_r(\text{target}) > \varepsilon_r(\text{background}) = \varepsilon_r(\text{air}) = 1. \tag{3.3}$$

Fig. 4(a) and (b) shows that, in this case, the backscattering signal should be basically one downward-looking peak. Therefore, we have selected on the experimental curve the first downward-looking peak with the largest amplitude. As to the rest of the experimental curve, it was set to zero. Hence, we work only with the selected peak.

Case 2. Suppose that the target is buried in the ground. In this case, we cannot claim the validity of (3.3). On the other hand, our numerical simulations (not shown here) have demonstrated that, if $\varepsilon_r(\text{target}) < \varepsilon_r(\text{background})$, then in the analog of Fig. 4(b), the peak would look upward. Therefore, in this case, we have selected on the experimental curve of the first peak with the largest amplitude to work with initially.

We were provided with five data sets. Fig. 6 shows superimposed preprocessed curves for all five targets we have worked with. The only peak that looks upward is the one for the plastic cylinder buried in soil since its dielectric constant was less than that of the soil (see Fig. 6). We stress once again that nothing was known in advance about the dielectric constants of targets. Therefore, the choice of the upward-looking peak in the case of the plastic cylinder was unbiased and was done only using the aforementioned rule. The measured amplitude for each case was on the order of 10^5. This is well above the amplitude in Fig. 4(b). Thus, all signals were preprocessed first (as previously described) and multiplied by the scaling number $SN = 10^{-7}$ next. Consider the LT of the simulated data shown in Fig. 4(b) and then the pre-processed signal for the bush (see Fig. 6) and multiply it by 10^{-7}. Fig. 7 depicts superimposed graphs of the function $\widehat{w}(0,s) = w(0,s) - w_0(0,s)$ for $s \in [1,5]$ for both cases. One can see that maximum and minimum values of both curves are approximately the same. We initially used $SN = 10^{-6}$, $SN = 10^{-7}$, and $SN = 10^{-8}$. Only for $SN = 10^{-7}$, the maximum and minimum values of functions $\widehat{w}(0,s)$ for $s \in [1,5]$ of both aforementioned curves, i.e., the one for the LT of the function depicted in Fig. 6 (bush), being multiplied by 10^{-7}, and the one for the LT of the function in Fig. 4(b), were approximately the same. On the other hand, those minimal and maximal values were quite different from the values of the LT of the function in Fig. 4(b) for $SN = 10^{-6}$ and $SN = 10^{-8}$. Using $SN = 10^{-7}$, which is based on the data for the bush, we have multiplied the other four preprocessed signals (see Fig. 6) by 10^{-7} and observed a similar behavior for the four other targets. For the case of the inverted peak in Fig. 6, we compared $|\widehat{w}(0,s)|$ for it with $\widehat{w}(0,s)$ for the aforementioned simulated data. Note that the signals shown in Fig. 6 are not yet multiplied by the scaling number. After multiplying these data by the scaling factor 10^{-7}, then for each set of experimental data, we took the resulting curve as the function $u(0,t) - u_0(0,t) := g(t) - u_0(0,t)$. Next, we worked only with this function as the data, using the aforementioned algorithm. For simple isolated targets, these steps of data preprocessing are justified, given the accuracy of the results obtained upon *a posteriori* inspection. For more complex target volumes, a more sophisticated analysis of sets of time histories will be necessary.

The data sets were processed, and the targets are illustrated in Fig. 5. If we compare the highly oscillatory curves of Fig. 5(b), (d) and (f), one can see that these backscatter time histories or signatures are qualitatively quite similar in appearance. Their oscillatory nature is due to the specific carrier frequency and

TABLE I
COMPUTED VALUES FOR R, THE RELATIVE DIELECTRIC CONSTANT IN (3.1), BASED ON BLIND PROCESSING OF MEASURED BACKSCATTER DATA FROM FIVE DIFFERENT TARGETS. HERE, A MEANS AIR, AND B MEANS DRY SAND

Target	A/B	R	ε_r (backgr)	ε_r (target) , calc.	ε_r (target) , published.
Figure 3.3-(a)	n/a	3.8	1	3.8	4 (known)
Bush	A	6.5	1	6.5	3 to 20 [10]
Wood stake	A	3.8	1	3.8	2 to 6 [21]
Metal box	B	3.8	3 to 5 [21]	11.4 to 19	10 to 30 (3.2)
Metal cylinder	B	4.3	3 to 5 [21]	12.9 to 21.4	10 to 30 (3.2)
Plastic cylinder	B	0.4	3 to 5 [21]	1.2 to 2	1.1 to 3.2 [21, 22]

finite bandwidth of the pulsed radiation, whereas the simulated data assume an idealized pulse. For these simple targets, we allow the aforementioned preprocessing step to force a correspondence between the two in order to identify the earliest return from the boundary of the target and determine its relative amplitude. Based on this, the inversion algorithm can determine a reliable estimate of that target's actual permittivity. In addition, we have conducted a limited sensitivity study with respect to the scaling factor. Specifically, we took $SN = 0.8 \cdot 10^{-7}$ and $SN = 1.2 \cdot 10^{-7}$ for all five targets, which are variations of 20% of the scaling number. In five out of five cases of experimental data, we have worked with values of R kept within tabulated limits (see Table I) when these variations of SN were tried. An optimal value of SN might be determined via a comparison of values of $R := R(SN)$ with measured values for a few known targets. At present, we have concentrated on reconstructing a real parameter that describes the permittivity of target features; and metal objects have been images simply having a very large relative permittivity. We note that there is no reason why a conductivity term could not be incorporated into the algorithm.

In addition to high oscillations of the data, we have faced two more uncertainties. First, we did not know where the time $t = 0$ is on our data. Second, we did not know where the actual location of the source x_0 is. This means that it is impossible to determine the location of the target. Hence, for computational purposes, we have arbitrarily assigned $t = 0$ to be a fixed location 1 ns off to the left from the beginning of the largest amplitude peak and $x_0 := -1$, knowing that we have independent GPS data to better fix absolute ranges should we need that information. Our primary objective here is to confirm the quantitative accuracy of the estimates of the dielectric constant of each of the targets, i.e., to accurately image the ratio R in (3.1).

The derivative of the LT of the preprocessed data was computed for $0 < s < 12$ with a step size of $\Delta s = 0.05$. Since the calculation of the derivative of noisy data is an ill-posed problem, we have used the following well-known formula for the calculation of the derivative of the LT:

$$\varphi'(s) - \partial_s w_0(0, s) = -\int_0^\infty (g(t) - u_0(0,t))\, te^{-st} dt. \quad (3.4)$$

Since for all targets the function $g(t) - u_0(0,t) = 0$ for $t > 2$ (see Fig. 6), then the integration in (3.4) is actually carried for $0 < t < 2$. We then define boundary conditions for functions $q_{n,k}$ for each n, and R is calculated by the aforementioned algorithm.

In Fig. 8(a) and (f), we regard R as the maximal amplitude of the calculated peak. We first verified that the algorithm provides a good estimate for R using simulated data. For the block in Fig. 4(a), we obtain the 1-D image shown in Fig. 8(a), which was found to be $\varepsilon_r = 3.8$, which is very close to the known value of 4. Next, we have calculated images from experimental data. In addition to Fig. 5(a), (c), and (e), we have also imaged two more cases, namely, a plastic cylinder and a metal cylinder, which are both buried in the ground with schematics similar with the one in Fig. 5(e). Fig. 8(b)–(f) displays our calculated images for all five targets.

Dielectric constants were not measured when the data were collected. Therefore, we have compared computed values of dielectric constants with those listed in tables [21], [22]. Note that these tables often provide a range of values rather than exact numbers; but given this caveat, the calculated results for these materials are well within the range of expectations (see Table I).

IV. CONCLUSION

We have described a new method for recovering quantitatively reliable estimates of target's material properties (dielectric constants) from backscatter field measurements. The method is an inverse scattering algorithm based on a rigorously formulated CIP. The numerical method is constructed to ensure global convergence, and therefore, it avoids stagnation at erroneous solutions for images of target permittivity distributions. Furthermore, the method requires no prior knowledge of the inhomogeneities present in the target volume. These properties are rigorously guaranteed. The authors are unaware of alternative numerical methods with similar characteristics for the case of the CIPs making use of such limited data.

The approach was evaluated here using data provided by the ARL from a forward-looking radar system without any prior knowledge of the targets being used. The data were measured using oblique incidence and with unknown source locations, and thus, some assumptions were made to provide the necessary inputs for the algorithm. The procedure first estimates a solution that has defined error given the quality of the data but which is guaranteed to be reliable. To simplify matters, only images of dielectric constants were recovered in order to validate the quantitative accuracy of the approach. Data sets were preprocessed, and a downrange permittivity profile was calculated. If the angular spread of backscatter time histories would be measured, then its additional processing would provide a 3-D image with a high spatial resolution, despite the use here of a single source point (see [7, Fig. 6.3]).

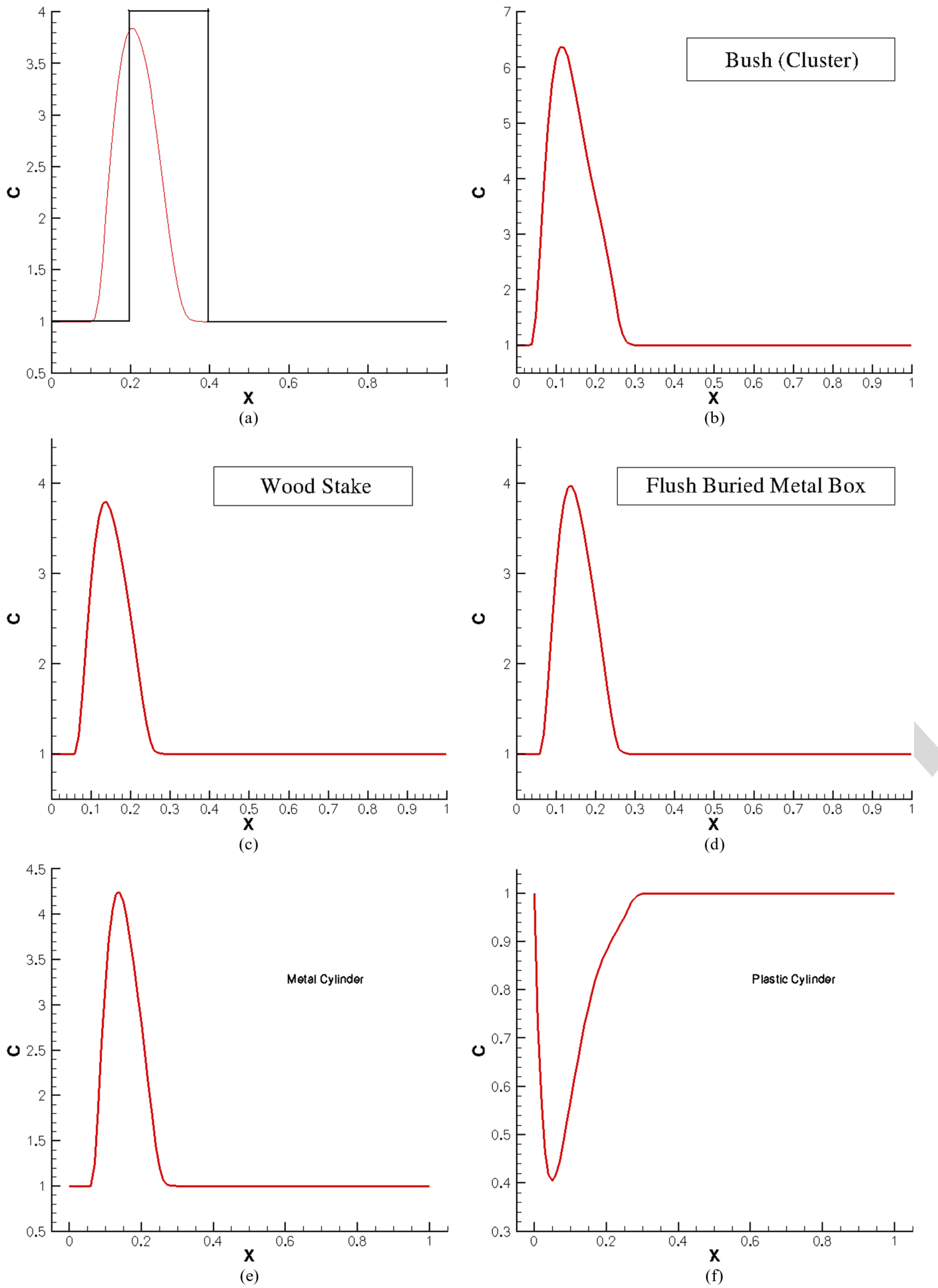

Fig. 8. Calculated images of targets. The ratio R in (3.1) is regarded as the maximal amplitude of the imaged peak. (a) Image for computationally simulated data as a verification of the accuracy of our algorithm. The rectangular block and the curve are true and computed profiles of the dielectric constant, respectively. The computed target/background contrast $R = 3.8$, which corresponds to a 5% of error. (b) Image of the bush [see Fig. 2(a)]. The calculated $\varepsilon_r(\text{bush}) = 6.5$, which is in the range of tabulated values $3 \le \varepsilon_r \le 20$ [10]. (c) Image of the wood stake [see Fig. 4(c)]. The calculated $\varepsilon_r(\text{wood stake}) = 3.8$ [10]. (d) Image of the buried metal box [see Fig. 5(e)]. The calculated $R = 3.8$. Since the background was dry sand with $3 \le \varepsilon_r(\text{dry sand}) \le 5$ [21], then the calculated ε_r (metal box) is between 11.4 and 19. This is within the range [see (3.2)] of appearing dielectric constants of metallic targets. (e) Calculated image of the buried metal cylinder. AQ9
The calculated ratio $R = 4.3$. Similarly with (d), we conclude that the calculated value of ε_r (metal cylinder) is between 12.9 and 21.4. This is again within the range [see (3.2)] of appearing dielectric constants of metallic targets. (f) Calculated image of the buried plastic cylinder. The calculated ratio $R = 0.4$. Similarly with (d), we conclude that the calculated value of the dielectric constant ε_r (plastic cylinder) is between 1.2 and 2.5, which is again within the range of tabulated values for plastic [21], [22].

Since the dielectric constants of the targets were not actually measured in the ARL experiments, then the best one can do is compare retrieved parameters with tabulated values. Table I shows the computed relative permittivities of targets. It is clearly shown that all five targets fall well within expected tabulated limits for the materials in question, despite the fact that no prior knowledge whatsoever was employed. We further emphasize that these results were obtained despite a very limited information content, large noise in the data, and significant discrepancies between experimental and simulated data. We can therefore conclude that these results point toward the validity of our mathematical model. The fact that regardless of limitations of the method, we consistently got results, which only later were found to fall well within tabulated limits, points toward a great degree of robustness of this algorithm.

The purpose of estimating the dielectric constant is to provide one extra piece of information about the target. Up to this point, most of the radar community has solely relied on the intensity of the radar image for doing detection and discrimination. It is anticipated that, when the intensity information is coupled with the new dielectric information this method provides, algorithms can be then designed that will provide better performance in terms of probability of detection and false alarm rates. Finally, we repeat that the results presented in this paper are primarily being used as a vehicle to illustrate this powerful inverse scattering algorithm method and its ability to recover dielectric properties of targets from experimental data collected by the forward-looking radar of the ARL. Detailed studies making use of larger experimental data sets from more complex 3-D scattering objects are necessary, and the authors will report on this in the near future.

References

[1] L. Beilina and C. Johnson, "A hybrid FEM/FDM method for an inverse scattering problem," in *Numerical Mathematics and Advanced Applications—ENUMATH 2001*. New York: Springer-Verlag, 2001.

[2] L. Beilina and C. Johnson, "A posteriori error estimation in computational inverse scattering," *Math. Models Methods Appl. Sci.*, vol. 15, no. 1, pp. 23–37, 2005.

[3] L. Beilina and M. V. Klibanov, "A globally convergent numerical method for a coefficient inverse problem," *SIAM J. Sci. Comput.*, vol. 31, no. 1, pp. 478–509, Oct. 2008.

[4] L. Beilina and M. V. Klibanov, "A posteriori error estimates for the adaptivity technique for the Tikhonov functional and global convergence for a coefficient inverse problem," *Inverse Probl.*, vol. 26, no. 4, pp. 045012-1–045012-27, Apr. 2010.

[5] L. Beilina, M. V. Klibanov, and M. Y. Kokurin, "Adaptivity with relaxation for ill-posed problems and global convergence for a coefficient inverse problem," *J. Math. Sci.*, vol. 167, no. 3, pp. 279–325, 2010.

[6] L. Beilina and M. V. Klibanov, "Reconstruction of dielectrics from experimental data via a hybrid globally convergent/adaptive algorithm," *Inverse Probl.*, vol. 26, no. 12, pp. 125 009-1–125 009-30, Dec. 2010.

[7] L. Beilina and M. V. Klibanov, *Approximate Global Convergence and Adaptivity for Coefficient Inverse Problems*. New York: Springer-Verlag, 2012.

[8] L. Beilina and M. V. Klibanov, "The philosophy of the approximate global convergence for multidimensional coefficient inverse problems," *Complex Variables Elliptic Equations*, to be published, to be published.

[9] H. Cao, M. V. Klibanov, and S. V. Pereverzev, "A Carleman estimate and the balancing principle in the quasi-reversibility method for solving the Cauchy problem for the Laplace equation," *Inverse Probl.*, vol. 25, no. 3, pp. 035005-1–035005-21, Mar. 2009.

[10] H. T. Chuah, K. Y. Lee, and T. W. Lau, "Dielectric constants of rubber and oil palm leaf samples at X-band," *IEEE Trans. Geosci. Remote Sens.*, vol. 33, no. 1, pp. 221–223, Jan. 1995.

[11] H. W. Engl, M. Hanke, and A. Neubauer, *Regularization of Inverse Problems*. Boston, MA: Kluwer, 2000.

[12] M. V. Klibanov, M. A. Fiddy, L. Beilina, N. Pantong, and J. Schenk, "Picosecond scale experimental verification of a globally convergent numerical method for a coefficient inverse problem," *Inverse Probl.*, vol. 26, no. 4, pp. 045003-1–045003-36, Apr. 2010.

[13] M. V. Klibanov and A. Timonov, *Carleman Estimates for Coefficient Inverse Problems and Numerical Applications*. Utrecht, The Netherlands: VSP, 2004.

[14] A. V. Kuzhuget and M. V. Klibanov, "Global convergence for a 1-D inverse problem with application to imaging of land mines," *Appl. Anal.*, vol. 89, no. 1, pp. 125–157, Jan. 2010.

[15] A. V. Kuzhuget, N. Pantong, and M. V. Klibanov, "A globally convergent numerical method for a coefficient inverse problem with backscattering data," *Methods Appl. Anal.*, vol. 18, pp. 47–68, 2011.

[16] A. V. Kuzhuget, L. Beilina, and M. V. Klibanov, "Approximate global convergence and quasi-reversibility for a coefficient inverse problem with backscattering data," *J. Math. Sci.*, vol. 181, no. 2, pp. 19–49, 2012.

[17] A. V. Kuzhuget, L. Beilina, M. V. Klibanov, A. Sullivan, L. Nguyen, and M. A. Fiddy, "Blind experimental data collected in the field and an approximately globally convergent inverse algorithm," *Inverse Probl.*, to be published, to be published.

[18] R. Lattes R and J.-L. Lions, *The Method of Quasireversibility: Applications to Partial Differential Equations*. New York: Elsevier, 1969.

[19] L. Nguyen, D. Wong, M. Ressler, F. Koenig, B. Stanton, G. Smith, J. Sichina, and K. Kappra, "Obstacle avolidance and concealed target detection using the Army Research Lab ultra-wideband synchronous impulse Reconstruction (UWB SIRE) forward imaging radar," in *Proc. SPIE*, 2007, vol. 6553, pp. 655 30H-1–655 30H-8.

[20] P. M. van den Berg, "Modified gradient and contrast source inversion," in *Analytical and Computational Methods in Scattering and Applied Mathematics*, F. Santosa and I. Stakgold, Eds. London, U.K.: Chapman & Hall, 2000, ch. 2.

[21] Tables of dielectric constants at. [Online]. Available: http://www.asiinstr.com/technical/Dielectric_Constants.htm

[22] Tables of dielectric constants at. [Online]. Available: http://www.krohne.com/Dielectric_Constants.6840.0.html

[23] A. N. Tikhonov, A. V. Goncharsky, V. V. Stepanov, and A. G. Yagola, *Numerical Methods for the Solution of Ill-Posed Problems*. Dordrecht, The Netherlands: Kluwer, 1995.

[24] Software package Wave Equations Solutions at. [Online]. Available: http://www.waves24.com/

Andrey V. Kuzhuget received the M.S. degree in mathematics from Novosibirsk State University, Novosibirsk, Russia, in 2006 and the Ph.D. degree in mathematics from University of North Carolina at Charlotte, Charlotte, in 2011.

Since 2011, he has been working with Morgan Stanley, New York, NY. His main research interest is in inverse problems for partial differential equations.

Larisa Beilina received the M.S. degree in mathematics from Latvian State University, Riga, Latvia, in 1992 and the Ph.D. degree in applied mathematics from Chalmers University of Technology, Gothenburg, Sweden, in 2003.

She was a Postdoctoral Fellow with Basel University, Basel, Switzerland, in 2003–2005 and with NTNU, Trondheim, Norway, in 2007–2008. Since 2009, she has been with the Department of Mathematical Sciences, Chalmers University of Technology and also with Gothenburg University, Gothenburg. Her main research interests are in adaptive finite-element methods and in inverse problems for partial differential equations.

Michael V. Klibanov received the M.S. degree in mathematics from Novosibirsk State University, Novosibirsk, Russia, in 1972, the Ph.D. degree in mathematics from Ural State University, Ekaterinburg, Russia, in 1977, and the D.Sc. degree from the Computing Center, Siberian Branch of Russian Academy of Science, Novosibirsk, in 1986.

Since 1990, he has been with the Department of Mathematics and Statistics, University of North Carolina at Charlotte, Charlotte. His main research interest is in inverse problems for partial differential equations.

Anders Sullivan received the B.S. and M.S. degrees in aerospace engineering from Georgia Institute of Technology, Atlanta, and the Ph.D. degree from Polytechnic University, Brooklyn, NY, with a specialty in electromagnetics.

He began his career with the U.S. Air Force Research Laboratory, Eglin Air Force Base, FL. Following this, he was a Postdoctoral Research Associate with the Electrical and Computer Engineering Department, Duke University, Durham, NC. He is currently a Senior Researcher with the U.S. Army Research Laboratory, Adelphi, MD. His main research interests include computational electromagnetics and ground-penetrating radar for landmine and IED detection applications.

Lam Nguyen received the B.S.E.E. degree from Virginia Polytechnic Institute, Blacksburg, the M.S.E.E degree from The George Washington University, Washington, DC, and the M.S.C.S degree from The Johns Hopkins University, Baltimore, MD.

He is currently a Team Lead with the RF Signal Processing and Modeling branch of the U.S. Army Research Laboratory, where he has primarily engaged in the research and development of several versions of UWB radar since early 1990s to present. These radar systems have been used for proof-of-concept demonstration in many concealed target detection programs. He has been developing algorithms for SAR signal and image processing. He has authored/coauthored over 80 conference, journal, and technical publications. He is a holder of two patents and has seven pending patents in SAR processing.

Mr. Nguyen was a recipient of the U.S. Army Research and Development Achievement Awards in 2006, 2008, and 2010.

Michael A. Fiddy received the Ph.D. degree in physics from the University of London, London, U.K., in 1977.

He was a Faculty Member with King's College London, London, U.K. In 1987, he moved to the University of Massachusetts Lowell, Lowell, where he was the ECE Department Head from 1994 to 2001. In January 2002, he was appointed the Founding Director of the Center for Optoelectronics and Optical Communications, University of North Carolina, Charlotte. His current research interests include inverse problems related to superresolution imaging and metamaterial design.

Dr. Fiddy is a Fellow of the Optical Society of America, the IOP, and The International Society for Optical Engineers. He has also been the Editor-in-Chief of the journal *Waves in Random and Complex Media* since 1996.

AUTHOR QUERIES

AUTHOR PLEASE ANSWER ALL QUERIES

Please be aware that the authors are required to pay overlength page charges ($200 per page) if the paper is longer than 6 pages. If you cannot pay any or all of these charges please let us know.

AQ1 = Morgan Stanley & Co. Inc. was changed to "Morgan Stanley." Please check if appropriate. Otherwise, please make the necessary changes.
AQ2 = Fig. 1 was not cited and was thus cited here. Please check if appropriate. Otherwise, please make the necessary changes.
AQ3 = Figures were renumbered. Please check.
AQ4 = "Above" in the portion "via the QRM, similarly with the above" was considered to be referring to the aforementioned equation. Please check if appropriate. Otherwise, please make the necessary changes.
AQ5 = "Below" in the portion "a 1-D example illustrated below" was considered to be referring to "Fig. 3." Please check if appropriate. Otherwise, please make the necessary changes.
AQ6 = "Remained" in the portion "values of R remained within tabulated limits" was changed to "kept." Please check if appropriate. Otherwise, please make the necessary changes.
AQ7 = The phrase "location one (1) nanosecond" was changed to "location 1 ns." Please check if appropriate. Otherwise, please make the necessary changes.
AQ8 = The phrase "1a image" in the portion "1a image shown in Fig. 8(a)" was change to "1-D image." Please check if appropriate. Otherwise, please make the necessary changes.
AQ9 = Equation (3.2) was inactively cited here. Please check if appropriate. Otherwise, please make the necessary changes.
AQ10 = Please provide publication update in Ref. [8].
AQ11 = Please provide publication update in Ref. [15].
AQ12 = Please provide publication update in Ref. [17].
AQ13 = Note that Ref. [21] has a web address that is not available. Please check.
AQ14 = Please provide the membership history of all authors.
AQ15 = The phrase "Postdoctoral positions" was changed to "Postdoctoral Fellow." Please check if appropriate. Otherwise, please make the necessary changes.
AQ16 = Please provide the expanded form of the abbreviation "NTNU."
AQ17 = Please provide the expanded form of the abbreviation "IED."
AQ18 = Please provide the expanded form of the abbreviation "UWB."
AQ19 = London University (King's College) was changed to "King's College London." Please check if appropriate. Otherwise, please make the necessary changes.
AQ20 = Please provide the expanded form of the abbreviation "ECE."
AQ21 = Please provide the expanded form of the abbreviation "IOP."

END OF ALL QUERIES

Quantitative Image Recovery From Measured Blind Backscattered Data Using a Globally Convergent Inverse Method

Andrey V. Kuzhuget, Larisa Beilina, Michael V. Klibanov, Anders Sullivan, Lam Nguyen, and Michael A. Fiddy

***Abstract*—The goal of this paper is to introduce the application of a globally convergent inverse scattering algorithm to estimate dielectric constants of targets using time-resolved backscattering data collected by a U.S. Army Research Laboratory forward-looking radar. The processing of the data was conducted blind, i.e., without any prior knowledge of the targets. The problem is solved by formulating the scattering problem as a coefficient inverse problem for a hyperbolic partial differential equation. The main new feature of this algorithm is its rigorously established global convergence property. Calculated values of dielectric constants are in a good agreement with material properties, which were revealed *a posteriori*.**

***Index Terms*—Experimental data, inverse scattering, quantitative imaging, remote sensing.**

I. Introduction

A FUNDAMENTAL problem in remote sensing is the processing of scattered field data from strongly scattering penetrable targets. Multiple scattering renders this problem extremely difficult to solve, it being ill conditioned with additional questions of uniqueness and, the most difficult, nonlinearity to contend with. In practice, limited noisy data typically require that some physical models be assumed, from which one hopes to extract meaningful and preferably quantitative information about the target in question. A number of recent publications by Beilina and Klibanov [3]–[8] and by Klibanov *et al.* [12], [14]–[16] have led to a new approach to address this important topic. This numerical method was originally developed for some multidimensional coefficient inverse problems (MCIPs) for a hyperbolic partial differential equation (PDE) using data from only a single location of either a point source or from a single direction of an incident plane wave. In particular, in [14], that method was extended from the 3-D case to the 1-D case. Thus, that 1-D version of [14] is used here to work with the experimental data. The illuminating field is pulsed in time, and the time history of the backscattering from the illuminated target volume constitutes the measured data that are processed by this algorithm. The authors are unaware of other groups working on MCIPs using data acquired from a single source location. However, the single measurement case is clearly the most practical one, particularly for military applications. Indeed, because of many dangers on the battlefield, the number of measurements should be minimized.

The algorithm in the aforementioned cited publications computes values for the spatial distribution of the dielectric constants of objects within the target volume. It is important to stress that this algorithm requires neither no prior knowledge of what might exist in the target volume nor a prior knowledge of a good first guess about the solution. There is a rigorous guarantee that this algorithm globally converges (see mathematical details in [7], [14], [16], and [17]). Because of the global convergence property, estimates of spatially distributed dielectric constants are reliable and systematically improve with more measured and less noisy data. The theory of the aforementioned cited publications rigorously guarantees that this numerical method delivers a good approximation to the exact solution of an MCIP without any *a priori* information about a small neighborhood of the exact solution as long as iterations start from the so-called "first tail function" $V_0(x)$, which can be easily computed using available boundary measurements (see (2.27)–(2.29) in Section II-C). In addition, it is in this sense that we use the term "global convergence" of the algorithm. The common perception of the term "global convergence" is that one can start from any point and still get the solution, but we stress that we actually start not from any point but rather from the function $V_0(x)$, which can be easily computed from the boundary data (see (2.27)–(2.29) in Section II-C).

It is well known that least squares functionals for MCIPs suffer from multiple local minima and ravines. Hence, local convergence of numerical methods to incorrect estimates will occur unless an initial guess that is close to the true solution is used. Such a guess is rarely available in most applications. In contrast, our algorithm does not use a least squares functional, and hence, it is free from the problem of local minima. Instead, this algorithm relies on the structure of the differential operator of the wave-like PDE.

Manuscript received March 24, 2012; revised July 22, 2012; accepted July 27, 2012. This work was supported in part by the U.S. Army Research Laboratory and the U.S. Army Research Office under Grant W911NF-11-1-0399; by the Swedish Research Council (VR); by the Swedish Foundation for Strategic Research (SSF) in Gothenburg Mathematical Modelling Centre; and by the Swedish Institute, Visby Program.

AQ1 A. V. Kuzhuget is with Morgan Stanley, New York, NY 10036 USA.

L. Beilina is with the Department of Mathematical Sciences, Chalmers University of Technology, 421 96 Gothenburg, Sweden, and also with Gothenburg University, 405 30 Gothenburg, Sweden (e-mail: larisa@chalmers.se).

M. V. Klibanov is with the Department of Mathematics and Statistics, University of North Carolina at Charlotte, Charlotte, NC 28223 USA (e-mail: mklibanv@uncc.edu).

A. Sullivan and L. Nguyen are with the U.S. Army Research Laboratory, Adelphi, MD 20783 USA (e-mail: anders.j.sullivan.civ@mail.mil; lam.h.nguyen2.civ@mail.mil).

M. A. Fiddy is with the Optoelectronics Center, University of North Carolina at Charlotte, Charlotte, NC 28223 USA (e-mail: mafiddy@uncc.edu).

Color versions of one or more of the figures in this paper are available online at http://ieeexplore.ieee.org.

Digital Object Identifier 10.1109/TGRS.2012.2211885

Prior to the work reported here, a major focus by the U.S. Army Research Laboratory (ARL) had been on the development of image processing techniques [19] that would improve radar images, which is through postprocessing techniques rather than through the application of inverse scattering methods. By incorporating more physics of the target-wave electromagnetic response into the data processing, one can greatly improve target detection and identification. Present data processing provides an electromagnetic field brightness or an intensity map of the target volume, which need not relate in a simple fashion to the scattering structures themselves. Our method estimates dielectric constants of targets, which obviously adds an important new dimension to the interpretation of data acquired by the radar system since this allows specific bounds on the dielectric properties of a feature in the target volume, which can help identify its likely material properties. Since no prior knowledge is required, the measured data were processed by Kuzhuget, Beilina, Klibanov, and Fiddy in the most challenging scenario, i.e., without any knowledge of the actual target structures and their dielectric properties. Once this had been done, Sullivan and Nguyen compared *a posteriori* the image estimates with the actually known material characteristics.

We draw attention to the fact that this algorithm has been used with forward-scattered data from experiments. These results were previously reported, which are also in a blind experiment (see [12, Tables 5 and 6] and [7, Tables 5.5 and 5.6]). In this case, the images in [12] were further improved and presented in a follow-up publication [6] using the adaptivity technique of [1], [2], [4], [5], and [7].

In Section II, we outline the basic steps in the underlying theory upon which the new algorithm is based. In Section III, we formulate the global convergence theorem. In Section IV, we outline results obtained using time-resolved backscatter electric field measurements collected in the field. Measurements were carried out by a forward-looking radar system built and operated by the ARL. The data were noisy and limited, and the target volumes included miscellaneous sources of clutter. The purpose of this particular radar system is to detect and possibly identify shallow explosive-like targets.

II. Theoretical Background

A. *Integral Differential Equation*

Since we were given only one time-resolved experimental curve per target, we had no choice but to use a 1-D mathematical model, although the reality is 3-D (see Section III for some details about the data collection). In addition, since only one component of the electric wave field was both transmitted and measured, we model the scattering process with one wave-like PDE rather than using complete Maxwell equations. We stress that the method is designed for use with 3-D problems, and one would normally collect data with co polarization and cross polarization in order to capture all of the pertinent information about the target. Here, we simply wish to show the steps employed by the method and demonstrate their quantitative reconstruction accuracy given noisy measured data.

We assume that the constitutive parameter of interest, i.e., mapping the target volume, is a relative permittivity $\varepsilon_r(x)$. In other words, we ignore magnetic effects in this paper. We also assume for convenience that $\varepsilon_r(x) = 1$ outside of the target volume, which is $x \in (0, 1)$ in our case. We assume that the source $x_0 < 0$ lies outside of the target volume. We can write the forward scattering problem as

$$\varepsilon_r(x)u_{tt} = u_{xx}, \qquad x \in \mathbb{R} \tag{2.1}$$
$$u(x,0) = 0, \quad u_t(x,0) = \delta(x - x_0). \tag{2.2}$$

The subscripts in (2.1) indicate the number of partial derivatives with respect to the variable indicated. The coefficient inverse problem (CIP) is to recover $\varepsilon_r(x)$, assuming that the initial illuminating pulse is known and that we measure the function $g(t)$, i.e.,

$$u(0,t) = g(t) \tag{2.3}$$

for sufficiently large times t that all multiple scattering events within the target volume, which can produce a measurable signal at the detector, do so. Practically, we gate the radiation source in time; and since the Laplace transform (LT), i.e., $w(x,s)$, is used to solve this CIP, the decay $e^{-st}, s > 0$ of the LT kernel further limits the duration of the measured time history. It is worth pointing out that, more typically, scattering data would be measured at different scattering angles for fixed frequency illumination at various incident angles. One can easily appreciate that this leads to the acquisition of Fourier information about the target or the secondary source function, depending upon the extent of the multiple scattering; and once one has sufficient data, a reasonable estimate of the target properties becomes possible. By taking measurements in the time domain, one can see that this is essentially simultaneously gathering information in a transform space from many illumination frequencies. The Laplace and Fourier transforms provide complimentary representations of the target in terms of moments or modes, respectively.

The LT is

$$w(x,s) = \int_0^\infty u(x,t)e^{-st}dt := \mathcal{L}u, \qquad s \geq \underline{s} = \text{const.} > 0 \tag{2.4}$$

and we assume that the so-called pseudofrequency $s \geq s(\varepsilon_r(x)) := \underline{s}$ is sufficiently large. This gives [7]

$$w_{xx} - s^2\varepsilon_r(x)w = -\delta(x - x_0), \qquad x \in \mathbb{R} \tag{2.5}$$
$$\lim_{|x|\to\infty} w(x,s) = 0. \tag{2.6}$$

Let

$$w(0,s) = \varphi(s) = \mathcal{L}g \tag{2.7}$$

be the LT of the measured function $g(t)$ in (2.3). Since $\varepsilon_r(x) = 1$ for $x < 0$, then, using (2.5) and (2.6), one can prove that, in addition to the function $w(0,s)$ in (2.7), the function $w_x(0,s)$ is also known as (see [17])

$$w_x(0,s) = s\varphi(s) - \exp(sx_0). \tag{2.8}$$

Let $w_0(x,s)$ be the solution of the problem in (2.5) and (2.6) for the case of the uniform background $\varepsilon_r(x) \equiv 1$. Then

$$w_0(x,s) = \frac{\exp(-s|x-x_0|)}{2s}. \tag{2.9}$$

When implementing the algorithm, given the assumption of a uniform normalized $\varepsilon_r(x) = 1$ outside of the target volume, we consider the function

$$r(x,s) = \frac{1}{s^2} \ln\left(\frac{w}{w_0}(x,s)\right). \tag{2.10}$$

Since the source $x_0 < 0$, then the function $r(x,s)$ is the solution of the following equation in the interval (0, 1):

$$r_{xx} + s^2 r_x^2 - 2sr_x = \varepsilon_r(x) - 1, \qquad x \in (0,1). \tag{2.11}$$

In addition, by (2.7) and (2.8)

$$r(0,s) = \varphi_0(s), \quad r_x(0,s) = \varphi_1(s) \tag{2.12}$$

$$\varphi_0(s) = \frac{\ln\varphi(s) - \ln(2s)}{s^2} + \frac{x_0}{s}$$
$$\varphi_1(s) = \frac{2}{s} - \frac{e^{sx_0}}{s^2\varphi(s)}. \tag{2.13}$$

The idea now is to eliminate the unknown coefficient $\varepsilon_r(x)$ from (2.11) via differentiation with respect to pseudofrequency s. Differentiating (2.11) with respect to s and denoting $q(x,s) = \partial_s r(x,s)$, we obtain

$$q_{xx} + 2s^2 q_x r_x + 2sr_x^2 - 2sq_x - 2r_x = 0, \qquad x \in (0,1). \tag{2.14}$$

We now need to express in (2.14) the function r via the function q. We have

$$r(x,s) = -\int_s^{\overline{s}} q(x,\tau)d\tau + V(x,\overline{s}) \tag{2.15}$$

where $V(x) := V(x,\overline{s})$ is referred to as the *tail function*, which is small in practice for large positive $\overline{s}$. Here, the truncation pseudofrequency $\overline{s}$ serves as a regularization parameter. The exact formula for $V(x)$ is

$$V(x,\overline{s}) := V(x) = r(x,\overline{s}) = \frac{1}{\overline{s}^2}\ln\left(\frac{w(x,\overline{s})}{w_0(x,\overline{s})}\right). \tag{2.16}$$

Substituting (2.15) in (2.14), we obtain the following nonlinear integral differential equation:

$$q_{xx} - 2s^2 q_x \int_s^{\overline{s}} q_x(x,\tau)d\tau + 2s\left[\int_s^{\overline{s}} q_x(x,\tau)d\tau\right]^2$$
$$- 2sq_x + 2\int_s^{\overline{s}} q_x(x,\tau)d\tau$$
$$+ 2s^2 q_x V_x - 4sV_x \int_s^{\overline{s}} q_x(x,\tau)d\tau$$
$$+ 2s(V_x)^2 - 2V_x = 0, \tag{2.17}$$
$$x \in (0,1); \quad s \in [\underline{s}, \overline{s}]$$

$$q(0,s) = \psi_0(s), \quad q_x(0,s) = \psi_1(s)$$
$$q_x(1,s) = 0, \qquad s \in [\underline{s}, \overline{s}] \tag{2.18}$$

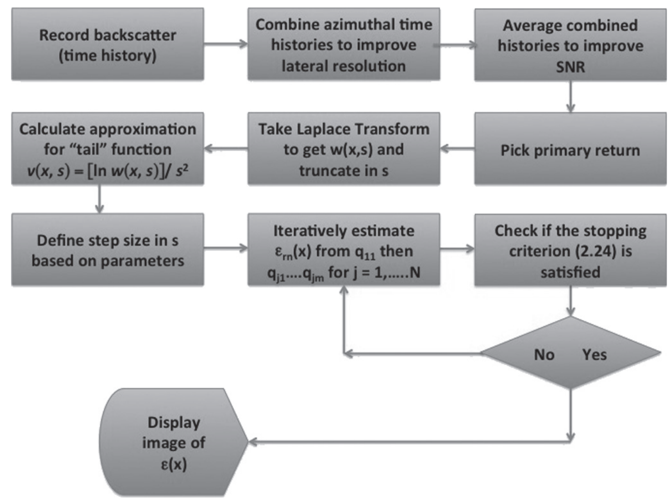

Fig. 1. Flowchart of the algorithm.

where functions $\psi_0(s) = \varphi_0'(s)$ and $\psi_1(s) = \varphi_1'(s)$ are derived from (2.13). The condition $q_x(1,s) = 0$ can be easily derived from (2.6) since $\varepsilon_r(x) = 1$ outside of the interval (0, 1).

In (2.17) and (2.18), both functions $q(x,s)$ and $V(x)$ are unknown. The reason why we can approximate both of them is that we find updates for $q(x,s)$ via inner iterations exploring (2.17) and (2.18) inside of the interval (0, 1). At the same time, we update the tail function $V(x)$ via outer iterations exploring the entire real line $\mathbb{R}$. In short, given an approximation for $V(x)$, the algorithm updates q and then updated for $\varepsilon_r(x)$. Next, the forward problem in (2.5) and (2.6) is solved for the function $w(x,s)$ for $s = \overline{s}$. Next, the tail function $V(x)$ is updated using (2.16). This might seem reminiscent of the steps in algorithms such as the modified gradient inverse scattering technique [20]; but we emphasize that, unlike our case, such methods have no global convergence properties.

B. Iterative Process

We now outline the formulation of our algorithm and the iterative process (see details in [7], [14], [16], and [17]; see Fig. 1). Unlike computationally simulated data in [14], we AQ2 do not use prior knowledge of the function $q(1,s)$ on the transmitted edge since this function is unknown to us. We have observed in our computational experiments that the knowledge of $q(1,s)$ only affects the accuracy of the calculation of the location of the target, but it does not affect the accuracy of the computed target/background contrast. Here, we are interested only in that contrast (see Section III). Since $\varepsilon_r(x) = 1$ for $x \geq 1$ and $x_0 < 0$, then one can easily derive from equations (2.5), (2.9), and (2.10) that $\partial_x q(1,s) = 0$.

Consider a partition of the interval $[\underline{s}, \overline{s}]$ into N small subintervals with the small grid step size $h > 0$ and assume that the function $q(x,s)$ is piecewise constant with respect to s. Thus

$$\underline{s} = s_N < s_{N-1} < \cdots < s_0 = \overline{s}, \qquad s_{i-1} - s_i = h$$
$$q(x,s) = q_n(x), \qquad \text{for } s \in (s_n, s_{n-1}]. \tag{2.19}$$

For each subinterval $(s_n, s_{n-1}]$ we obtain a differential equation for the function $q_n(x)$. We assign, for convenience of notations, $q_0 :\equiv 0$. Following the aforementioned idea of a combination of inner and outer iterations, we perform for each n inner iterations

with respect to the tail function. This way, we obtain functions $q_{n,k}$ and $V_{n,k}$. The equation for the pair $(q_{n,k}, V_{n,k})$ is

$$q''_{n,k} - \left(A_{1,n} h \sum_{j=0}^{n-1} q'_j - A_{1,n} V'_{n,k} - 2A_{2,n} \right) q'_{n,k}$$
$$= -A_{2,n} h^2 \left(\sum_{j=0}^{n-1} q'_j \right)^2 + 2h \sum_{j=0}^{n-1} q'_j + 2A_{2,n} V'_{n,k} \left(h \sum_{j=0}^{n-1} q'_j \right)$$
$$- A_{2,n} \left(V'_{n,k} \right)^2 + 2A_{2,n} V'_{n,k}, \qquad x \in (0,1) \tag{2.20}$$
$$q_{n,k}(0) = \psi_{0,n}, \quad q'_{n,k}(0) = \psi_{1,n}, \quad q'_{n,k}(1) = 0 \tag{2.21}$$
$$\psi_{0,n} = \frac{1}{h} \int_{s_n}^{s_{n-1}} \psi_0(s) ds, \quad \psi_{1,n} = \frac{1}{h} \int_{s_n}^{s_{n-1}} \psi_1(s) ds.$$

Here, $A_{1,n}$ and $A_{2,n}$ are certain numbers, whose exact expressions are given in [3] and [7].

The choice of the first tail function $V_0(x)$ is described in Section II-C. Let $n \geq 1$. Suppose that, for $j = 0, \ldots n-1$, functions $q_j(x)$ and $V_j(x)$ are already constructed. We now need to construct functions $q_{n,k}$ and $V_{n,k}$ for $k = 1, \ldots, m$. We set $V_{n,1}(x) := V_{n-1}(x)$. Next, using the quasi-reversibility method (QRM) (see Section II-C), we approximately solve (2.20) for $k = 1$ with overdetermined boundary conditions in (2.21) and find the function $q_{n,1}$. Next, we find the approximation $\varepsilon_r^{(n,1)}$ for the unknown coefficient $\varepsilon_r(x)$ via the following two formulas:

$$r_{n,1}(x) = -hq_{n,1} - h \sum_{j=0}^{n-1} q_j + V_{n,1}, \qquad x \in [0,1] \tag{2.22}$$
$$\varepsilon_r^{(n,1)}(x) = 1 + r''_{n,1}(x) + s_n^2 \left[r'_{n,1}(x) \right]^2 - 2s_n r'_{n,1}(x), \qquad x \in [0,1]. \tag{2.23}$$

Next, we solve the forward problem in (2.5) and (2.6) with $\varepsilon_r(x) := \varepsilon_r^{(n,1)}(x)$, $\;s := \overline{s}$ and find the function $w_{n,1}(x, \overline{s})$ this way. After this, we update the tail via the formula in (2.16), in which $w(x, \overline{s}) := w_{n,1}(x, \overline{s})$. This way, we obtain a new tail $V_{n,2}(x)$. Similarly, we continue iterating with respect to tails m times. Next, we set

$$q_n(x) := q_{n,m}(x),\ V_n(x) := V_{n,m}(x),\ \varepsilon_r^{(n)}(x) := \varepsilon_r^{(n,m)}(x)$$

replace n with $n+1$ and repeat this process. We continue this process until [15]

$$\text{either } \left\| \varepsilon_r^{(n)} - \varepsilon_r^{(n-1)} \right\|_{L_2(0,1)} \leq 10^{-5} \quad \text{or } \left\| \nabla J_\alpha(q_{n,k}) \right\|_{L_2(0,1)} \geq 10^5 \tag{2.24}$$

where the functional $J_\alpha(q_{n,k})$ is defined in Section II-C. Here, the norm in the space $L_2(0,1)$ is understood in the discrete sense. In the case when the second inequality in (2.24) is satisfied, we stop at the previous iteration, taking $\varepsilon_r^{(n,k-1)}(x)$ as our solution. If neither of two conditions in (2.24) is not reached at $n := N$, then we repeat the aforementioned sweep over the interval $[\underline{s}, \overline{s}]$, taking the pair $(q_N(x), V_N(x))$ as the new pair $(q_0(x), V_0(x))$. Usually, at least one of the conditions in (2.24) is reached either on the third or on the fourth sweep, and the process stops then. AQ3

C. Computing Functions $q_{n,k}(x)$ and $V_0(x)$

At first glance, it seems that, for a given tail function $V_{n,k}(x)$, the function $q_{n,k}(x)$ can be computed as the solution of a conventional boundary value problem for the ordinary differential equation in (2.20) with any two out of three boundary conditions in (2.21). However, attempts to do so led to poor quality images (see [14, Remark 3.1]). At the same time, the QRM has resulted in accurate solutions both in [14] and in Test 1 for synthetic data (see succeeding discussion). The QRM is well designed to compute least squares solutions of PDEs with overdetermined boundary conditions, such as, e.g., the problem in (2.20) and (2.21). We refer to [18] for the originating work about the QRM and to [7], [9], [13], [15], and [16] for some follow-up publications.

Let $L(q_{n,k})(x)$ and $P_{n,k}(x)$ be left- and right-hand sides of (2.20), respectively. In our numerical studies, $L(q_{n,k})(x)$ and $P_{n,k}(x)$ are written in the form of finite differences. Let $\alpha \in (0,1)$ be the regularization parameter. The QRM minimizes the following Tikhonov regularization functional:

$$J_\alpha(q_{n,k}) = \| L_{n,k}(q_{n,k}) - P_{n,k} \|^2_{L_2(0,1)} + \alpha \| q_{n,k} \|^2_{H^2(0,1)} \tag{2.25}$$

subject to boundary conditions in (2.21). Here, again norms in $L_2(0,1)$ and in the Sobolev space $H^2(0,1)$ are understood in the discrete sense. The functional $J_\alpha(q_{n,k})$ in (2.25) is quadratic. Using this fact and the tool of Carleman estimates, it can be shown that $J_\alpha(q_{n,k})$ has a unique global minimum and no local minima [14], [15], [17]. We find that global minimum via the conjugate gradient method, minimizing with respect to the values of the function $q_{n,k}$ at grid points. We have used 100 grid points in the interval (0, 1). The step size in the s-direction was $h = 0.5$. The s-interval was $[\underline{s}, \overline{s}] = [3, 12]$. For each $n = 1, \ldots, N$, we take functions $q_{n,k}$ for $k = 1, \ldots m$, and we typically choose $m = 10$. The reason for the choice of $m = 10$ is that numerical experience has shown that, for each of the n, tails stabilize at $k \approx 10$. As to the regularization parameter α, we have found, when testing synthetic data, that $\alpha = 0.04$ is the optimal one, and we take it in our computations.

We note that we determined the regularization parameter when testing simulated data. These data were for the target depicted in Fig. 7(a), for which we varied the regularization parameter between 0.03 and 0.05. The resulting images for these data showed only an insignificant change. We also varied the regularization parameter between 0.03 and 0.05 for the experimental data. Again, we only observed insignificant changes, which lead us to select the average value of 0.04. Although the regularization theory states that the regularization parameter should depend on the noise level in the data [23], we do not actually know the noise level for our data. Further, for nonlinear problems (as we have), this dependence is claimed by regularization theory only for the limiting case of a relatively small level of noise, which is not our case. In our computations using measured data, one works with some level of noise, which is not likely to be small and is unknown. Therefore, in practice, when applying this algorithm to experimental data, we were guided by results from simulations to choose a value for the regularization parameter. If we had prior knowledge about some objects in the target volume, then we would choose the optimal

regularization parameter for that object. Because we processed the data without any prior knowledge whatsoever about the objects, we chose the regularization parameter based on the simulated data processing, and fortunately, our answers for five out of five targets were well within tabulated limits.

We now describe an important step in choosing the first tail function $V_0(x)$. To choose it, we consider the asymptotic behavior of the function $V(x,\overline{s})$ in (2.16) with respect to the truncation pseudofrequency $\overline{s} \to \infty$. This behavior is [14], [17]

$$V(x,\overline{s}) = \frac{p_0(x)}{\overline{s}} + O\left(\frac{1}{\overline{s}^2}\right), \qquad \overline{s} \to \infty.$$

We truncate the term $O(1/\overline{s}^2)$, which is somewhat similar with the defining of geometrical optics as a high-frequency approximation of the solution of the Helmholtz equation. Hence, we take

$$V(x,\overline{s}) \approx \frac{p_0(x)}{\overline{s}}.$$

Since $q = \partial_s r$ and $V(x,\overline{s}) = r(x,\overline{s})$, then

$$q(x,\overline{s}) = -\frac{p_0(x)}{\overline{s}^2}. \qquad (2.26)$$

Hence, setting in (2.17) $s := \overline{s}$ and using (2.26), we obtain the following *approximate* equation for the function $p_0(x)$:

$$\frac{d^2}{dx^2} p_0(x) = 0, \qquad x \in (0,1). \qquad (2.27)$$

Boundary conditions for $p_0(x)$ can be easily derived from (2.18) and (2.26) as

$$p_0(0) = -\overline{s}^2 \psi_0(\overline{s}),\ p_0'(0) = -\overline{s}^2 \psi_1(\overline{s}),\ p_0'(1) = 0. \qquad (2.28)$$

We find an approximate solution $p_{0,appr}(x)$ of the problem in (2.27) and (2.28) via the QRM, similarly with the aforementioned equation. Next, we set for the first tail function, i.e., AQ4

$$V_0(x) := \frac{p_{0,appr}(x)}{\overline{s}}. \qquad (2.29)$$

A simplified formal statement of the global convergence theorem is as follows (see [7, Th. 6.1] for more details and [7, Th. 6.7] for the 3-D case).

Theorem 1: Let the function $\varepsilon_r^*(x)$ be the exact solution of our CIP for the noiseless data $g^*(t)$ in (2.3). Fix the truncation pseudofrequency $\overline{s} > 1$. Let the first tail function $V_0(x)$ be defined via (2.27)–(2.29). Let $\sigma \in (0,1)$ be the level of the error in the boundary data, i.e.,

$$|\psi_0(s) - \psi_0^*(s)| \le \sigma,\ |\psi_1(s) - \psi_1^*(s)| \le \sigma, \qquad \text{for } s \in [\underline{s}, \overline{s}]$$

where functions $\psi_0(s)$ and $\psi_1(s)$ depend on the function $g(t)$ in (2.3) via (2.7), (2.13) and (2.18); and functions $\psi_0^*(s)$ and $\psi_1^*(s)$ depend on the noiseless data $g^*(t)$ in the same way. Let $h \in (0,1)$ be the grid step size in the s-direction in (2.19); let $\sqrt{\alpha} = \sigma$ and $\widetilde{h} = \max(\sigma, h)$. Let Q be the total number of functions $\varepsilon_r^{(n,k)}$ computed in the aforementioned algorithm. Then, there exists a constant $D = D(x_0, d, \overline{s}) > 1$ such that, if the numbers σ and h are so small, that

$$\widetilde{h} < \frac{1}{D^{2Q+2}} \qquad (2.30)$$

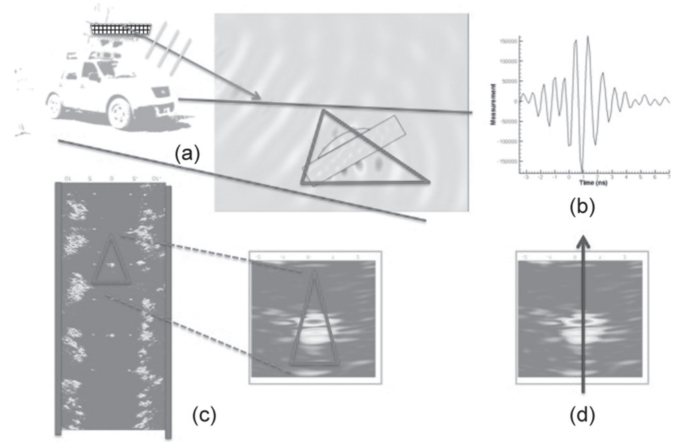

Fig. 2. (a) Schematic diagram of the forward-looking radar system illuminating a dielectric target. (b) Typical measured time history of the backscatter field. (c) Composite of unprocessed returns highlighting the dielectric target (indicated by the red triangle). (d) Downrange cut of the permittivity profile, which the new algorithm will generate.

then the following estimate is valid:

$$\left\| \varepsilon_r^{(n,k)} - \varepsilon_r^* \right\|_{L_2(0,1)} \le \widetilde{h}^{\omega} \qquad (2.31)$$

where the number $\omega \in (0,1)$ is independent of n, k, $\widetilde{h}$, $\varepsilon_r^{(n,k)}$, and ε_r^*.

Therefore, Theorem 1 guarantees that, if the total number Q of computed functions $\varepsilon_r^{(n,k)}$ is fixed and error parameters σ, h are sufficiently small, then obtained iterative solutions $\varepsilon_r^{(n,k)}(x)$ are sufficiently close to the exact solution ε_r^*,; and this closeness is defined by the error parameters. Therefore, the total number of iterations Q can be considered as the regularization parameter of our process, which is the additional regularization parameter to the number $\overline{s}$. The combination of inequalities in (2.30) and (2.31) has a direct analog in the inequality in [11, Lemma 6.2, p. 156] for classical Landweber iterations, which are defined for a substantially different ill-posed problem. As to the total number of iterations Q being a regularization parameter here, there is no surprise in this. Indeed, it is stated on [11, p. 157] that the number of iterations can serve as a regularization parameter for an ill-posed problem.

III. Imaging Results

The schematic of the data collection by the forward-looking radar is shown in Fig. 2(a). Time-resolved electromagnetic pulses are emitted by two sources installed on the radar. Only one component of the electric field is both transmitted and measured in the backscatter direction. The data are collected by sixteen detectors with the step size in time of 0.133 ns. Data from shallow targets placed both below and above the ground were provided. The only piece of information provided by the ARL team (Sullivan and Nguyen) to Kuzhuget, Beilina, Klibanov, and Fiddy was whether the target was located above the ground or was buried. The depth of the upper surface of a buried target was a few centimeters. GPS was used to provide the distance between the radar and a point on the ground, which is located above that target to within a few centimeters error.

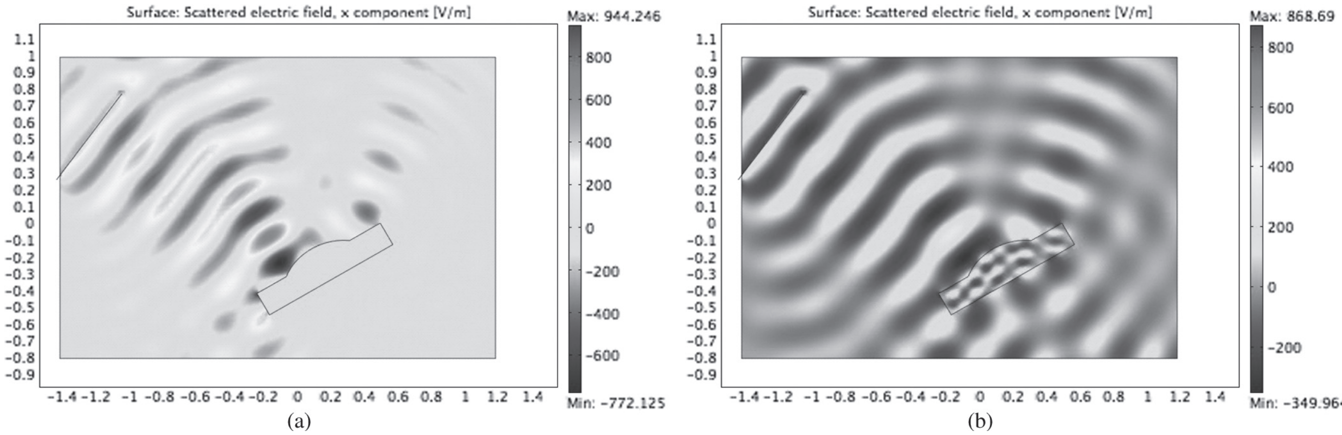

Fig. 3. (a) Scattered field from a metallic target. (b) Scattered field from a high-permittivity target with the same shape ($\varepsilon_r(\text{target}) = 10$). Note the similarity between the backscatter electric fields in cases (a) and (b).

The time-resolved voltages induced by the backreflected signals were integrated over the radar to target distances ranging from 8 to 20 m, and they were also averaged with respect to both source positions and with respect to the output of the 16 detectors. Since we can assume here that the radar/target distance was known, then it was also approximately known which part of the measured time-resolved signal would correspond to scattering events from that target (see Fig. 2). Despite the presence of clutter, a single time-dependent curve is extracted from the measured return time histories, as illustrated in Fig. 2(b). This is the form of the data that have been processed in each of the five measured data sets generated by the ARL. A typical plot of returns without applying the inverse algorithm is shown in Fig. 2(c), where the triangle denotes a possible target of interest among the clutter from the backscatter generated from the volume of the region illuminated by the radar in Fig. 2(a). We process a set of averaged time histories like those shown in Fig. 2(b) to create a down-range cut of the permittivity profile, as indicated in Fig. 2(d).

Our objective was to calculate ratios

$$R = \frac{\varepsilon_r(\text{target})}{\varepsilon_r(\text{background})} \tag{3.1}$$

of dielectric constants. If the $\varepsilon_r(\text{background})$ is known, then it is trivial to deduce $\varepsilon_r(\text{target})$. Clearly, for a target located above the ground, $\varepsilon_r(\text{background}) = 1$. In general, we would expect the target volume to contain many inhomogeneities with spatially varying $\varepsilon_r(x)$. A weighted average of dielectric constants of these constituent materials will be found over the volume spatial resolution cell that corresponds to the particular data acquisition configuration. In the examples presented here, we show results obtained from just one time-history curve for each target, corresponding to one polarization component of the incident electromagnetic field and backscatter data measured and averaged over all 16 receiver locations. Clearly, this severely limits the transverse resolution but improves the signal-to-noise ratio for 1-D imaging in the propagation direction. The model is further simplified by using the 1-D CIP employing only one hyperbolic PDE. Consequently, the interpretation of the backscattering radiation will assign a high-permittivity value to metal structures. A comparison between Fig. 3(a) and (b) illustrates this. We use the upper bound $\varepsilon_r(\text{target}) = 30$ for the metallic targets because our calculations show that LT in (2.7), from the response function $g(t)$, almost coincides for $\varepsilon_r(\text{target}) \geq 30$.

In both cases of a metal structure and a high-permittivity structure, one can expect enhanced backscatter if the incident pulse includes frequencies that correspond to a normal mode of the target. Hence, we assign

$$10 \leq \varepsilon_r(\text{metallic target}) \leq 30. \tag{3.2}$$

We call (3.2) the appearing dielectric constant of metallic targets. In other words, we consider in (3.2) that regions appearing to have a high dielectric constant could also be metallic targets.

To appreciate the kind of backscatter data and image recovery expected from a simple dielectric block, a 1-D example illustrated in Fig. 3 was investigated. Computations in this example were performed using the software package WavES [24]. The permittivity profile, i.e., $\varepsilon_r(\text{target}) = 4$, is shown in Fig. 4(a); and the computed function $u(0,t) = g(t)$ for $0 < t < 3$ is shown in Fig. 4(b) [see (2.3) for $g(t)$]. We assume temporal units here for which at $t = 3$, a distance of $x = 3$ units is traversed; the source is at $x_0 = -1$, and the block's front face is at $x = 0.2$. Since the block is 0.2 units wide, $g(t)$ represents the backscatter return from the front and back face of the block. The reason why, in Fig. 4(b), $g(t) = 0$ for $t < 1$ and $g(t) = 1/2$ for $1 \leq t \leq 1.4$ is that the solution of the problem in (2.1) and (2.2) for $\varepsilon_r(x) \equiv 1$ is $u_0(x,t) = H(t - |x - x_0|)/2$, where $H(z)$ is the Heaviside function, i.e.,

$$H(z) = \begin{cases} 0, z < 0 \\ 1, z \geq 0. \end{cases}$$

Hence, $u(0,t) = g(t) = H(t-1)/2$ for $1 \leq t \leq 1.4$; and at $t = 1.4$, the return wave from the block hits the observation point $\{x = 0\}$ for the first time.

The measured data are also challenging to process since they arise from oblique illumination, and the exact location and the amplitudes of the incident pulses were not known. In addition, a comparison of Fig. 4(b) with Fig. 5(b), (d), and (f) shows that the measured data are highly oscillatory, which are unlike their simulated counterparts. Consequently, we applied

AQ5

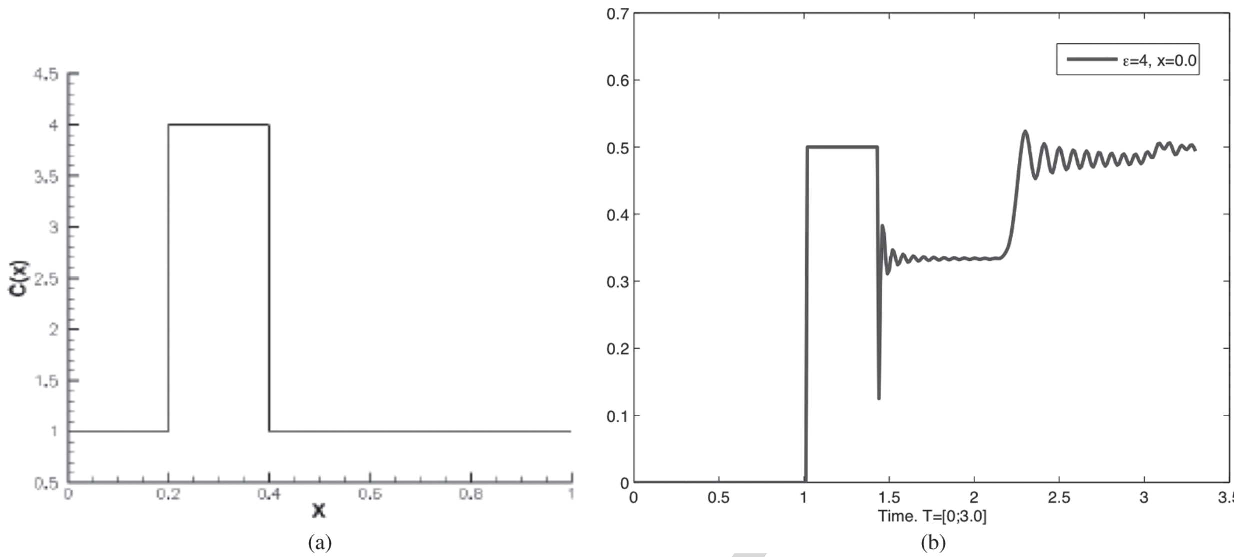

Fig. 4. (a) Function $\varepsilon_r(\text{target}) = 4$; note that $\varepsilon_r(\text{background}) = 1$. (b) $u(0,t) = g(t)$ for $0 < t < 3.0$. The source is located at $x_0 = -1$, and the first backscatter return is therefore shown at approximately $t = 2.4$ with "ringing" determined by interference of multiply scattered waves between the two boundaries of the block. Computations were performed using the software package WavES [24].

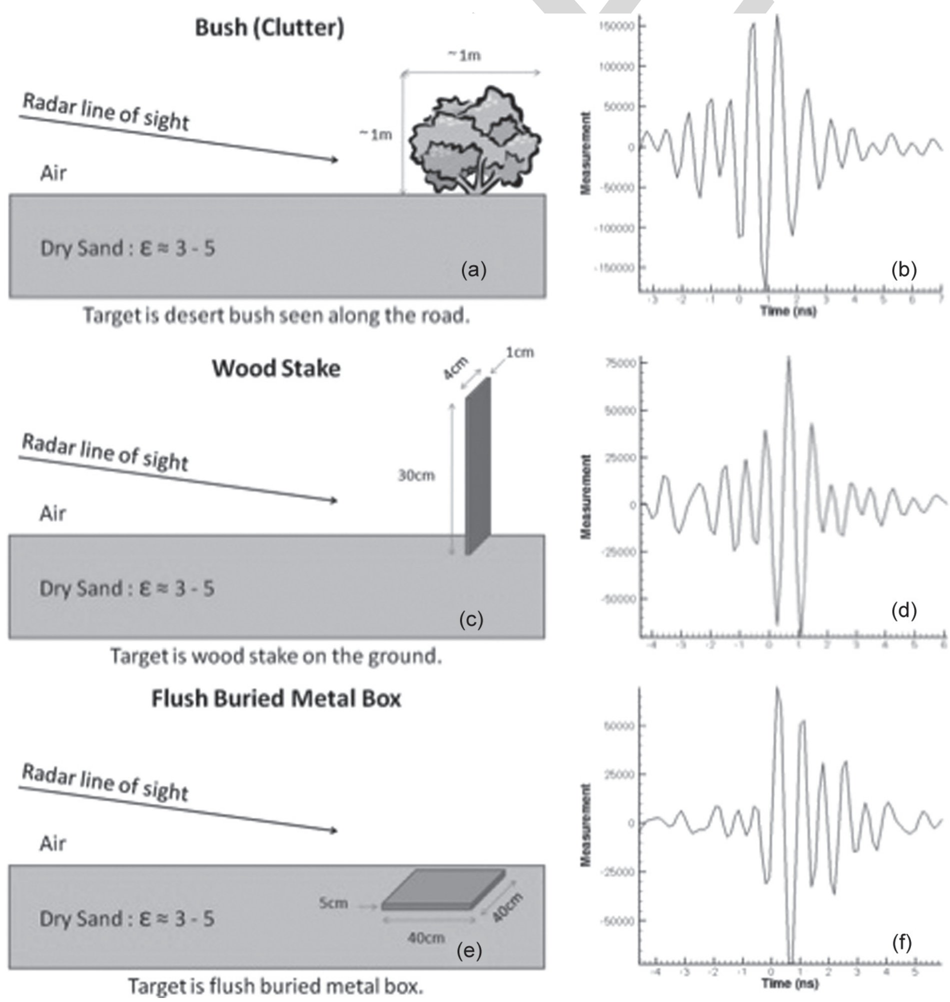

Fig. 5. Three targets and their associated measured data. The ground is dry sand with $3 \leq \varepsilon_r \leq 5$ [21], [22]. The information shown in (a), (c), and (e) were only provided after computations were made. (a) Depicts a bush that was located on a road, which generated background clutter. (b) Scaled experimental data for (a), where the horizontal axis represents time in nanoseconds having a time step of 0.133 ns; and the vertical axis is the amplitude of the measured voltage at the detector. (c) Wooden stake. (d) Scaled experimental data for (c). (e) Metal box buried in dry sand. (f) Scaled experimental data for (e). The mismatch between experimental and simulated data [see Fig. 4(b)] is evident.

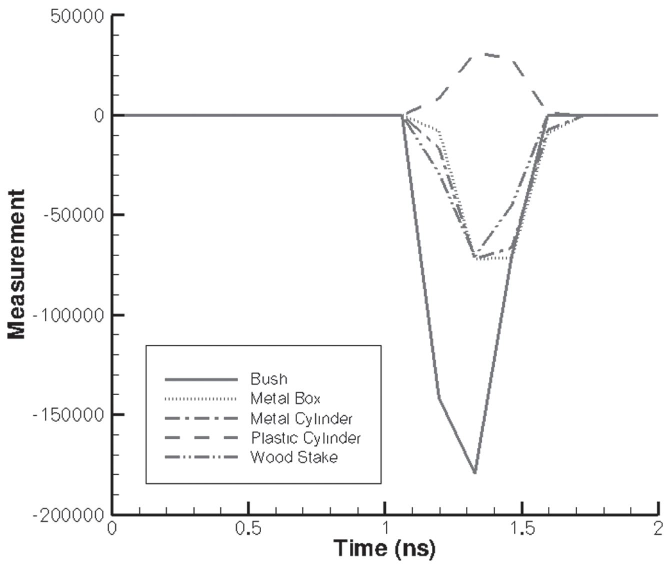

Fig. 6. Superimposed preprocessed data for all five cases under consideration. The upward-looking peak corresponds to the plastic cylinder (see Table I).

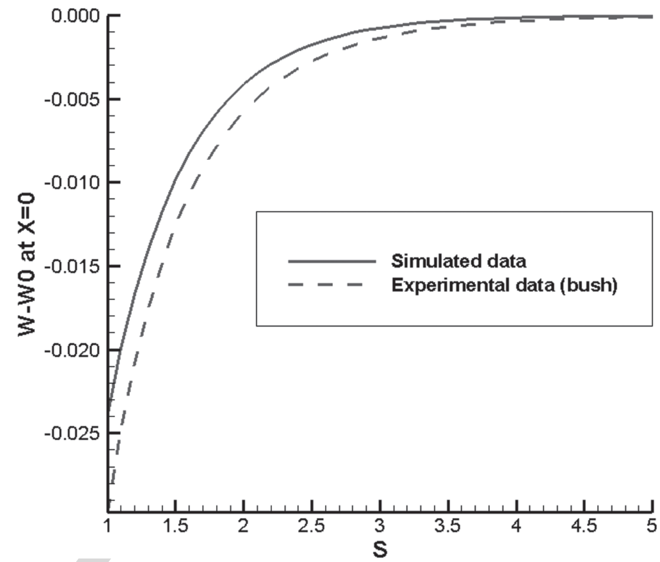

Fig. 7. Graphs of the function $\widehat{w}(0,s) = w(0,s) - w_0(0,s)$ for $s \in [1,5]$ for the LT of the computationally simulated data in Fig. 4(b) and of the preprocessed signal for the bush (see Fig. 6). The signal in Fig. 6 for the bush was multiplied by 10^{-7}. Minimal and maximal values of the function $\widehat{w}(0,s)$ are similar for both curves. A similar observation was made for four other targets we have worked with.

an intuitively reasonable data preprocessing procedure, which remained totally unbiased since it was applied to blind data sets. The idea of this procedure is to make the data more similar to that shown in Fig. 4(b). Previously, a similar procedure was reported for transmitted data in [6], [7], and [12]. We have considered two cases.

Case 1. Suppose that the target is located above the ground. In this case

$$\varepsilon_r(\text{target}) > \varepsilon_r(\text{background}) = \varepsilon_r(\text{air}) = 1. \quad (3.3)$$

Fig. 4(a) and (b) shows that, in this case, the backscattering signal should be basically one downward-looking peak. Therefore, we have selected on the experimental curve the first downward-looking peak with the largest amplitude. As to the rest of the experimental curve, it was set to zero. Hence, we work only with the selected peak.

Case 2. Suppose that the target is buried in the ground. In this case, we cannot claim the validity of (3.3). On the other hand, our numerical simulations (not shown here) have demonstrated that, if $\varepsilon_r(\text{target}) < \varepsilon_r(\text{background})$, then in the analog of Fig. 4(b), the peak would look upward. Therefore, in this case, we have selected on the experimental curve of the first peak with the largest amplitude to work with initially.

We were provided with five data sets. Fig. 6 shows superimposed preprocessed curves for all five targets we have worked with. The only peak that looks upward is the one for the plastic cylinder buried in soil since its dielectric constant was less than that of the soil (see Fig. 6). We stress once again that nothing was known in advance about the dielectric constants of targets. Therefore, the choice of the upward-looking peak in the case of the plastic cylinder was unbiased and was done only using the aforementioned rule. The measured amplitude for each case was on the order of 10^5. This is well above the amplitude in Fig. 4(b). Thus, all signals were preprocessed first (as previously described) and multiplied by the scaling number $SN = 10^{-7}$ next. Consider the LT of the simulated data shown in Fig. 4(b) and then the pre-processed signal for the bush (see Fig. 6) and multiply it by 10^{-7}. Fig. 7 depicts superimposed graphs of the function $\widehat{w}(0,s) = w(0,s) - w_0(0,s)$ for $s \in [1,5]$ for both cases. One can see that maximum and minimum values of both curves are approximately the same. We initially used $SN = 10^{-6}$, $SN = 10^{-7}$, and $SN = 10^{-8}$. Only for $SN = 10^{-7}$, the maximum and minimum values of functions $\widehat{w}(0,s)$ for $s \in [1,5]$ of both aforementioned curves, i.e., the one for the LT of the function depicted in Fig. 6 (bush), being multiplied by 10^{-7}, and the one for the LT of the function in Fig. 4(b), were approximately the same. On the other hand, those minimal and maximal values were quite different from the values of the LT of the function in Fig. 4(b) for $SN = 10^{-6}$ and $SN = 10^{-8}$. Using $SN = 10^{-7}$, which is based on the data for the bush, we have multiplied the other four preprocessed signals (see Fig. 6) by 10^{-7} and observed a similar behavior for the four other targets. For the case of the inverted peak in Fig. 6, we compared $|\widehat{w}(0,s)|$ for it with $\widehat{w}(0,s)$ for the aforementioned simulated data. Note that the signals shown in Fig. 6 are not yet multiplied by the scaling number. After multiplying these data by the scaling factor 10^{-7}, then for each set of experimental data, we took the resulting curve as the function $u(0,t) - u_0(0,t) := g(t) - u_0(0,t)$. Next, we worked only with this function as the data, using the aforementioned algorithm. For simple isolated targets, these steps of data preprocessing are justified, given the accuracy of the results obtained upon *a posteriori* inspection. For more complex target volumes, a more sophisticated analysis of sets of time histories will be necessary.

The data sets were processed, and the targets are illustrated in Fig. 5. If we compare the highly oscillatory curves of Fig. 5(b), (d) and (f), one can see that these backscatter time histories or signatures are qualitatively quite similar in appearance. Their oscillatory nature is due to the specific carrier frequency and

TABLE I
COMPUTED VALUES FOR R, THE RELATIVE DIELECTRIC CONSTANT IN (3.1), BASED ON BLIND PROCESSING OF MEASURED BACKSCATTER DATA FROM FIVE DIFFERENT TARGETS. HERE, A MEANS AIR, AND B MEANS DRY SAND

Target	A/B	R	ε_r (backgr)	ε_r (target) , calc.	ε_r (target) , published.
Figure 3.3-(a)	n/a	3.8	1	3.8	4 (known)
Bush	A	6.5	1	6.5	3 to 20 [10]
Wood stake	A	3.8	1	3.8	2 to 6 [21]
Metal box	B	3.8	3 to 5 [21]	11.4 to 19	10 to 30 (3.2)
Metal cylinder	B	4.3	3 to 5 [21]	12.9 to 21.4	10 to 30 (3.2)
Plastic cylinder	B	0.4	3 to 5 [21]	1.2 to 2	1.1 to 3.2 [21, 22]

finite bandwidth of the pulsed radiation, whereas the simulated data assume an idealized pulse. For these simple targets, we allow the aforementioned preprocessing step to force a correspondence between the two in order to identify the earliest return from the boundary of the target and determine its relative amplitude. Based on this, the inversion algorithm can determine a reliable estimate of that target's actual permittivity. In addition, we have conducted a limited sensitivity study with respect to the scaling factor. Specifically, we took $SN = 0.8 \cdot 10^{-7}$ and $SN = 1.2 \cdot 10^{-7}$ for all five targets, which are variations of 20% of the scaling number. In five out of five cases of experimental data, we have worked with values of R kept within tabulated limits (see Table I) when these variations of SN were tried. An optimal value of SN might be determined via a comparison of values of $R := R(SN)$ with measured values for a few known targets. At present, we have concentrated on reconstructing a real parameter that describes the permittivity of target features; and metal objects have been images simply having a very large relative permittivity. We note that there is no reason why a conductivity term could not be incorporated into the algorithm.

In addition to high oscillations of the data, we have faced two more uncertainties. First, we did not know where the time $t = 0$ is on our data. Second, we did not know where the actual location of the source x_0 is. This means that it is impossible to determine the location of the target. Hence, for computational purposes, we have arbitrarily assigned $t = 0$ to be a fixed location 1 ns off to the left from the beginning of the largest amplitude peak and $x_0 := -1$, knowing that we have independent GPS data to better fix absolute ranges should we need that information. Our primary objective here is to confirm the quantitative accuracy of the estimates of the dielectric constant of each of the targets, i.e., to accurately image the ratio R in (3.1).

The derivative of the LT of the preprocessed data was computed for $0 < s < 12$ with a step size of $\Delta s = 0.05$. Since the calculation of the derivative of noisy data is an ill-posed problem, we have used the following well-known formula for the calculation of the derivative of the LT:

$$\varphi'(s) - \partial_s w_0(0,s) = -\int_0^\infty (g(t) - u_0(0,t))\, te^{-st} dt. \quad (3.4)$$

Since for all targets the function $g(t) - u_0(0,t) = 0$ for $t > 2$ (see Fig. 6), then the integration in (3.4) is actually carried for $0 < t < 2$. We then define boundary conditions for functions $q_{n,k}$ for each n, and R is calculated by the aforementioned algorithm.

In Fig. 8(a) and (f), we regard R as the maximal amplitude of the calculated peak. We first verified that the algorithm provides a good estimate for R using simulated data. For the block in Fig. 4(a), we obtain the 1-D image shown in Fig. 8(a), which was found to be $\varepsilon_r = 3.8$, which is very close to the known value of 4. Next, we have calculated images from experimental data. In addition to Fig. 5(a), (c), and (e), we have also imaged two more cases, namely, a plastic cylinder and a metal cylinder, which are both buried in the ground with schematics similar with the one in Fig. 5(e). Fig. 8(b)–(f) displays our calculated images for all five targets.

Dielectric constants were not measured when the data were collected. Therefore, we have compared computed values of dielectric constants with those listed in tables [21], [22]. Note that these tables often provide a range of values rather than exact numbers; but given this caveat, the calculated results for these materials are well within the range of expectations (see Table I).

IV. CONCLUSION

We have described a new method for recovering quantitatively reliable estimates of target's material properties (dielectric constants) from backscatter field measurements. The method is an inverse scattering algorithm based on a rigorously formulated CIP. The numerical method is constructed to ensure global convergence, and therefore, it avoids stagnation at erroneous solutions for images of target permittivity distributions. Furthermore, the method requires no prior knowledge of the inhomogeneities present in the target volume. These properties are rigorously guaranteed. The authors are unaware of alternative numerical methods with similar characteristics for the case of the CIPs making use of such limited data.

The approach was evaluated here using data provided by the ARL from a forward-looking radar system without any prior knowledge of the targets being used. The data were measured using oblique incidence and with unknown source locations, and thus, some assumptions were made to provide the necessary inputs for the algorithm. The procedure first estimates a solution that has defined error given the quality of the data but which is guaranteed to be reliable. To simplify matters, only images of dielectric constants were recovered in order to validate the quantitative accuracy of the approach. Data sets were preprocessed, and a downrange permittivity profile was calculated. If the angular spread of backscatter time histories would be measured, then its additional processing would provide a 3-D image with a high spatial resolution, despite the use here of a single source point (see [7, Fig. 6.3]).

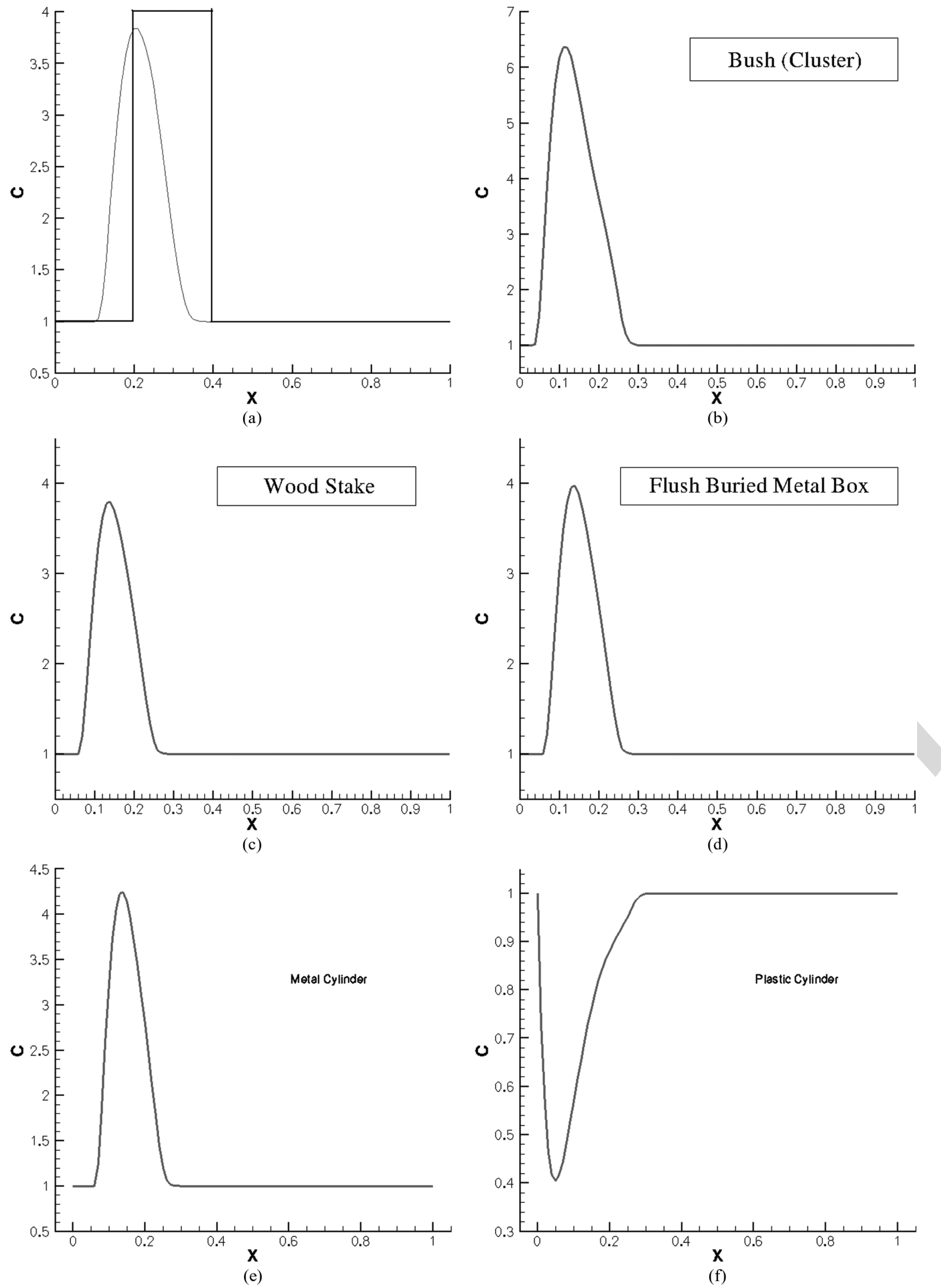

Fig. 8. Calculated images of targets. The ratio R in (3.1) is regarded as the maximal amplitude of the imaged peak. (a) Image for computationally simulated data as a verification of the accuracy of our algorithm. The rectangular block and the curve are true and computed profiles of the dielectric constant, respectively. The computed target/background contrast $R = 3.8$, which corresponds to a 5% of error. (b) Image of the bush [see Fig. 2(a)]. The calculated $\varepsilon_r(\text{bush}) = 6.5$, which is in the range of tabulated values $3 \leq \varepsilon_r \leq 20$ [10]. (c) Image of the wood stake [see Fig. 4(c)]. The calculated $\varepsilon_r(\text{wood stake}) = 3.8$ [10]. (d) Image of the buried metal box [see Fig. 5(e)]. The calculated $R = 3.8$. Since the background was dry sand with $3 \leq \varepsilon_r(\text{dry sand}) \leq 5$ [21], then the calculated ε_r (metal box) is between 11.4 and 19. This is within the range [see (3.2)] of appearing dielectric constants of metallic targets. (e) Calculated image of the buried metal cylinder. AQ9
The calculated ratio $R = 4.3$. Similarly with (d), we conclude that the calculated value of ε_r (metal cylinder) is between 12.9 and 21.4. This is again within the range [see (3.2)] of appearing dielectric constants of metallic targets. (f) Calculated image of the buried plastic cylinder. The calculated ratio $R = 0.4$. Similarly with (d), we conclude that the calculated value of the dielectric constant ε_r (plastic cylinder) is between 1.2 and 2.5, which is again within the range of tabulated values for plastic [21], [22].

Since the dielectric constants of the targets were not actually measured in the ARL experiments, then the best one can do is compare retrieved parameters with tabulated values. Table I shows the computed relative permittivities of targets. It is clearly shown that all five targets fall well within expected tabulated limits for the materials in question, despite the fact that no prior knowledge whatsoever was employed. We further emphasize that these results were obtained despite a very limited information content, large noise in the data, and significant discrepancies between experimental and simulated data. We can therefore conclude that these results point toward the validity of our mathematical model. The fact that regardless of limitations of the method, we consistently got results, which only later were found to fall well within tabulated limits, points toward a great degree of robustness of this algorithm.

The purpose of estimating the dielectric constant is to provide one extra piece of information about the target. Up to this point, most of the radar community has solely relied on the intensity of the radar image for doing detection and discrimination. It is anticipated that, when the intensity information is coupled with the new dielectric information this method provides, algorithms can be then designed that will provide better performance in terms of probability of detection and false alarm rates. Finally, we repeat that the results presented in this paper are primarily being used as a vehicle to illustrate this powerful inverse scattering algorithm method and its ability to recover dielectric properties of targets from experimental data collected by the forward-looking radar of the ARL. Detailed studies making use of larger experimental data sets from more complex 3-D scattering objects are necessary, and the authors will report on this in the near future.

References

[1] L. Beilina and C. Johnson, "A hybrid FEM/FDM method for an inverse scattering problem," in *Numerical Mathematics and Advanced Applications—ENUMATH 2001*. New York: Springer-Verlag, 2001.

[2] L. Beilina and C. Johnson, "A posteriori error estimation in computational inverse scattering," *Math. Models Methods Appl. Sci.*, vol. 15, no. 1, pp. 23–37, 2005.

[3] L. Beilina and M. V. Klibanov, "A globally convergent numerical method for a coefficient inverse problem," *SIAM J. Sci. Comput.*, vol. 31, no. 1, pp. 478–509, Oct. 2008.

[4] L. Beilina and M. V. Klibanov, "A posteriori error estimates for the adaptivity technique for the Tikhonov functional and global convergence for a coefficient inverse problem," *Inverse Probl.*, vol. 26, no. 4, pp. 045012-1–045012-27, Apr. 2010.

[5] L. Beilina, M. V. Klibanov, and M. Y. Kokurin, "Adaptivity with relaxation for ill-posed problems and global convergence for a coefficient inverse problem," *J. Math. Sci.*, vol. 167, no. 3, pp. 279–325, 2010.

[6] L. Beilina and M. V. Klibanov, "Reconstruction of dielectrics from experimental data via a hybrid globally convergent/adaptive algorithm," *Inverse Probl.*, vol. 26, no. 12, pp. 125 009-1–125 009-30, Dec. 2010.

[7] L. Beilina and M. V. Klibanov, *Approximate Global Convergence and Adaptivity for Coefficient Inverse Problems*. New York: Springer-Verlag, 2012.

[8] L. Beilina and M. V. Klibanov, "The philosophy of the approximate global convergence for multidimensional coefficient inverse problems," *Complex Variables Elliptic Equations*, to be published, to be published. AQ10

[9] H. Cao, M. V. Klibanov, and S. V. Pereverzev, "A Carleman estimate and the balancing principle in the quasi-reversibility method for solving the Cauchy problem for the Laplace equation," *Inverse Probl.*, vol. 25, no. 3, pp. 035005-1–035005-21, Mar. 2009.

[10] H. T. Chuah, K. Y. Lee, and T. W. Lau, "Dielectric constants of rubber and oil palm leaf samples at X-band," *IEEE Trans. Geosci. Remote Sens.*, vol. 33, no. 1, pp. 221–223, Jan. 1995.

[11] H. W. Engl, M. Hanke, and A. Neubauer, *Regularization of Inverse Problems*. Boston, MA: Kluwer, 2000.

[12] M. V. Klibanov, M. A. Fiddy, L. Beilina, N. Pantong, and J. Schenk, "Picosecond scale experimental verification of a globally convergent numerical method for a coefficient inverse problem," *Inverse Probl.*, vol. 26, no. 4, pp. 045003-1–045003-36, Apr. 2010.

[13] M. V. Klibanov and A. Timonov, *Carleman Estimates for Coefficient Inverse Problems and Numerical Applications*. Utrecht, The Netherlands: VSP, 2004.

[14] A. V. Kuzhuget and M. V. Klibanov, "Global convergence for a 1-D inverse problem with application to imaging of land mines," *Appl. Anal.*, vol. 89, no. 1, pp. 125–157, Jan. 2010.

[15] A. V. Kuzhuget, N. Pantong, and M. V. Klibanov, "A globally convergent numerical method for a coefficient inverse problem with backscattering data," *Methods Appl. Anal.*, vol. 18, pp. 47–68, 2011. AQ11

[16] A. V. Kuzhuget, L. Beilina, and M. V. Klibanov, "Approximate global convergence and quasi-reversibility for a coefficient inverse problem with backscattering data," *J. Math. Sci.*, vol. 181, no. 2, pp. 19–49, 2012.

[17] A. V. Kuzhuget, L. Beilina, M. V. Klibanov, A. Sullivan, L. Nguyen, and M. A. Fiddy, "Blind experimental data collected in the field and an approximately globally convergent inverse algorithm," *Inverse Probl.*, to be published, to be published. AQ12

[18] R. Lattes R and J.-L. Lions, *The Method of Quasireversibility: Applications to Partial Differential Equations*. New York: Elsevier, 1969.

[19] L. Nguyen, D. Wong, M. Ressler, F. Koenig, B. Stanton, G. Smith, J. Sichina, and K. Kappra, "Obstacle avolidance and concealed target detection using the Army Research Lab ultra-wideband synchronous impulse Reconstruction (UWB SIRE) forward imaging radar," in *Proc. SPIE*, 2007, vol. 6553, pp. 655 30H-1–655 30H-8.

[20] P. M. van den Berg, "Modified gradient and contrast source inversion," in *Analytical and Computational Methods in Scattering and Applied Mathematics*, F. Santosa and I. Stakgold, Eds. London, U.K.: Chapman & Hall, 2000, ch. 2.

[21] Tables of dielectric constants at. [Online]. Available: http://www.asiinstr.com/technical/Dielectric_Constants.htm AQ13

[22] Tables of dielectric constants at. [Online]. Available: http://www.krohne.com/Dielectric_Constants.6840.0.html

[23] A. N. Tikhonov, A. V. Goncharsky, V. V. Stepanov, and A. G. Yagola, *Numerical Methods for the Solution of Ill-Posed Problems*. Dordrecht, The Netherlands: Kluwer, 1995.

[24] Software package Wave Equations Solutions at. [Online]. Available: http://www.waves24.com/

Andrey V. Kuzhuget received the M.S. degree in mathematics from Novosibirsk State University, Novosibirsk, Russia, in 2006 and the Ph.D. degree in mathematics from University of North Carolina at Charlotte, Charlotte, in 2011. AQ14

Since 2011, he has been working with Morgan Stanley, New York, NY. His main research interest is in inverse problems for partial differential equations.

Larisa Beilina received the M.S. degree in mathematics from Latvian State University, Riga, Latvia, in 1992 and the Ph.D. degree in applied mathematics from Chalmers University of Technology, Gothenburg, Sweden, in 2003.

She was a Postdoctoral Fellow with Basel University, Basel, Switzerland, in 2003–2005 and with NTNU, Trondheim, Norway, in 2007–2008. Since 2009, she has been with the Department of Mathematical Sciences, Chalmers University of Technology and also with Gothenburg University, Gothenburg. Her main research interests are in adaptive finite-element methods and in inverse problems for partial differential equations.

Michael V. Klibanov received the M.S. degree in mathematics from Novosibirsk State University, Novosibirsk, Russia, in 1972, the Ph.D. degree in mathematics from Ural State University, Ekaterinburg, Russia, in 1977, and the D.Sc. degree from the Computing Center, Siberian Branch of Russian Academy of Science, Novosibirsk, in 1986.

Since 1990, he has been with the Department of Mathematics and Statistics, University of North Carolina at Charlotte, Charlotte. His main research interest is in inverse problems for partial differential equations.

Anders Sullivan received the B.S. and M.S. degrees in aerospace engineering from Georgia Institute of Technology, Atlanta, and the Ph.D. degree from Polytechnic University, Brooklyn, NY, with a specialty in electromagnetics.

He began his career with the U.S. Air Force Research Laboratory, Eglin Air Force Base, FL. Following this, he was a Postdoctoral Research Associate with the Electrical and Computer Engineering Department, Duke University, Durham, NC. He is currently a Senior Researcher with the U.S. Army Research Laboratory, Adelphi, MD. His main research interests include computational AQ17 electromagnetics and ground-penetrating radar for landmine and IED detection applications.

Lam Nguyen received the B.S.E.E. degree from Virginia Polytechnic Institute, Blacksburg, the M.S.E.E degree from The George Washington University, Washington, DC, and the M.S.C.S degree from The Johns Hopkins University, Baltimore, MD.

He is currently a Team Lead with the RF Signal Processing and Modeling branch of the U.S. Army Research Laboratory, where he has primarily engaged in the research and development of several versions of UWB radar since early 1990s to present. AQ18 These radar systems have been used for proof-of-concept demonstration in many concealed target detection programs. He has been developing algorithms for SAR signal and image processing. He has authored/coauthored over 80 conference, journal, and technical publications. He is a holder of two patents and has seven pending patents in SAR processing.

Mr. Nguyen was a recipient of the U.S. Army Research and Development Achievement Awards in 2006, 2008, and 2010.

Michael A. Fiddy received the Ph.D. degree in physics from the University of London, London, U.K., in 1977.

He was a Faculty Member with King's College London, London, U.K. In 1987, he moved to the University AQ19 of Massachusetts Lowell, Lowell, where he was the ECE Department Head from 1994 to 2001. AQ20 In January 2002, he was appointed the Founding Director of the Center for Optoelectronics and Optical Communications, University of North Carolina, Charlotte. His current research interests include inverse problems related to superresolution imaging and metamaterial design.

Dr. Fiddy is a Fellow of the Optical Society of America, the IOP, and The AQ21 International Society for Optical Engineers. He has also been the Editor-in-Chief of the journal *Waves in Random and Complex Media* since 1996.

AUTHOR QUERIES

AUTHOR PLEASE ANSWER ALL QUERIES

Please be aware that the authors are required to pay overlength page charges ($200 per page) if the paper is longer than 6 pages. If you cannot pay any or all of these charges please let us know.

AQ1 = Morgan Stanley & Co. Inc. was changed to “Morgan Stanley.” Please check if appropriate. Otherwise, please make the necessary changes.
AQ2 = Fig. 1 was not cited and was thus cited here. Please check if appropriate. Otherwise, please make the necessary changes.
AQ3 = Figures were renumbered. Please check.
AQ4 = “Above” in the portion “via the QRM, similarly with the above” was considered to be referring to the aforementioned equation. Please check if appropriate. Otherwise, please make the necessary changes.
AQ5 = “Below” in the portion “a 1-D example illustrated below” was considered to be referring to “Fig. 3.” Please check if appropriate. Otherwise, please make the necessary changes.
AQ6 = “Remained” in the portion “values of R remained within tabulated limits” was changed to “kept.” Please check if appropriate. Otherwise, please make the necessary changes.
AQ7 = The phrase “location one (1) nanosecond” was changed to “location 1 ns.” Please check if appropriate. Otherwise, please make the necessary changes.
AQ8 = The phrase “1a image” in the portion “1a image shown in Fig. 8(a)” was change to “1-D image.” Please check if appropriate. Otherwise, please make the necessary changes.
AQ9 = Equation (3.2) was inactively cited here. Please check if appropriate. Otherwise, please make the necessary changes.
AQ10 = Please provide publication update in Ref. [8].
AQ11 = Please provide publication update in Ref. [15].
AQ12 = Please provide publication update in Ref. [17].
AQ13 = Note that Ref. [21] has a web address that is not available. Please check.
AQ14 = Please provide the membership history of all authors.
AQ15 = The phrase “Postdoctoral positions” was changed to “Postdoctoral Fellow.” Please check if appropriate. Otherwise, please make the necessary changes.
AQ16 = Please provide the expanded form of the abbreviation “NTNU.”
AQ17 = Please provide the expanded form of the abbreviation “IED.”
AQ18 = Please provide the expanded form of the abbreviation “UWB.”
AQ19 = London University (King’s College) was changed to “King’s College London.” Please check if appropriate. Otherwise, please make the necessary changes.
AQ20 = Please provide the expanded form of the abbreviation “ECE.”
AQ21 = Please provide the expanded form of the abbreviation “IOP.”

END OF ALL QUERIES